

<https://doi.org/10.1038/s42003-025-07752-2>

TMEM106B deficiency leads to alterations in lipid metabolism and obesity in the TDP-43^{Q331K} knock-in mouse model

Cha Yang¹, Gwang Bin Lee², Ling Hao² & Fenghua Hu¹

The *TMEM106B* gene, encoding a lysosomal membrane protein, is closely linked with brain aging and neurodegeneration. *TMEM106B* has been identified as a risk factor for several neurodegenerative diseases characterized by aggregation of the RNA-binding protein TDP-43, including frontotemporal lobar degeneration (FTLD) and limbic-predominant age-related TDP-43 encephalopathy (LATE). To investigate the role of TMEM106B in TDP-43 proteinopathy, we ablated TMEM106B in the TDP-43^{Q331K} knock-in mouse line, which expresses an ALS-linked TDP-43 mutation at endogenous levels. We found that TMEM106B deficiency leads to glial activation, Purkinje cell loss, and behavioral deficits in TDP-43^{Q331K} mice without inducing typical TDP-43 pathology. Interestingly, ablation of TMEM106B results in significant body weight gain, increased fat deposition, and hepatic triglyceride (TG) accumulation in TDP-43^{Q331K} mice. In addition, lipidomic and transcriptome analysis shows a profound alteration in lipid metabolism in the liver of TDP-43^{Q331K} *Tmem106b*^{-/-} mice. Our studies reveal a novel function of TMEM106B and TDP-43 in lipid metabolism and provide new insights into their roles in neurodegeneration.

TAR DNA-binding protein 43 (TDP-43) proteinopathy, typically characterized by the presence of aberrant cytoplasmic aggregation and nuclear loss of TDP-43, is a prominent pathological feature of many neurodegenerative diseases^{1–4}, including amyotrophic lateral sclerosis (ALS)^{1,5}, frontotemporal lobar degeneration (FTLD)^{1,6,7}, Alzheimer's disease (AD)^{8–10}, Huntington's diseases (HD)¹¹, and a recently recognized disease entity, limbic-predominant age-related TDP-43 encephalopathy (LATE)^{12,13}. However, molecular pathways leading to TDP-43 proteinopathy are still poorly understood.

Recent studies have found *TMEM106B*, a gene encoding a lysosomal membrane protein, as a genetic risk factor for several diseases with TDP-43 proteinopathy, including FTLD with *GRN* mutations^{7,14–16} and LATE¹². Additionally, *TMEM106B* is associated with FTLD with *C9ORF72* mutations^{17–20}, chronic traumatic encephalopathy (CTE)^{21,22}, hippocampal sclerosis in aging (HS-Aging)^{23,24}, and brain aging²⁵. Moreover, a dominant D252N mutation in *TMEM106B* causes hypomyelinating leukodystrophy (HLD)^{26,27}. Intriguingly, TMEM106B C-terminal fragments (CTFs) have been recently discovered to form amyloid fibrils in aged brains and brains of patients suffering from neurodegenerative disorders^{28–34}. As a lysosomal transmembrane protein, TMEM106B regulates several aspects of lysosomal function, including lysosomal morphology^{35–38}, lysosome pH^{38–40}, lysosomal enzyme activity^{39,41}, lysosome exocytosis⁴⁰, lysosomal positioning⁴², and

lysosomal trafficking in dendrites⁴³ and axons^{41,44,45}. Moreover, TMEM106B has been predicted to be a lipid transfer protein⁴⁶, indicating a possible role of TMEM106B in lipid metabolism.

In FTLD with *GRN* mutations^{7,14–16} and LATE¹², the TMEM106B risk allele is associated with more TDP-43 pathology. A recent study further showed that the rs3173615 risk allele of TMEM106B exhibits lower levels of TMEM106B dimer, higher levels of TMEM106B CTF fibrils, and exacerbated TDP-43 dysfunction⁴⁷. However, in ALS patients the minor protective allele of TMEM106B, correlated with lower TMEM106B levels, was found to correlate with more TDP-43 pathology⁴⁸. In addition, partial loss of TMEM106B was found to cause cytoplasmic aggregation of TDP-43 in cell culture⁴⁸. Thus, how TMEM106B regulates TDP-43 aggregation, in particular, whether TMEM106B loss of function or gain of toxicity from TMEM106B CTF fibrils facilitates TDP-43 aggregation remains to be elucidated. In this study, we utilize a TDP-43 mouse model expressing an ALS-associated TDP-43 mutation at endogenous levels (TDP-43^{Q331K}) to investigate the role of TMEM106B in TDP-43 proteinopathy. We found that TMEM106B deficiency leads to exacerbated behavioral deficits and pathological changes in the brain in TDP-43^{Q331K} mice without disturbing TDP-43 homeostasis. Surprisingly, we found that TDP-43^{Q331K} *Tmem106b*^{-/-} mice develop obesity with a drastic alteration in lipid composition and lipid metabolism. Our study reveals an unexpected role of

¹Department of Molecular Biology and Genetics, Weill Institute for Cell and Molecular Biology, Cornell University, Ithaca, NY, USA. ²Department of Chemistry and Biochemistry, University of Maryland, College Park, MD, US. ✉ e-mail: fh87@cornell.edu

TMEM106B in lipid metabolism and provides new insights into the functions of TMEM106B and TDP-43 in neurodegeneration.

Results

TMEM106B deficiency does not induce TDP-43 pathology in TDP-43^{Q331K} mice

Mutations in TDP-43 have been genetically linked to ALS and FTLD^{49–51}. Mice expressing the ALS-linked TDP-43 mutant Q331K (TDP-43^{Q331K}) at the endogenous TDP-43 loci do not display typical TDP-43 pathology, such as cytoplasmic aggregation and nuclear loss of TDP-43, but show increased TDP-43 levels as a result of the perturbed autoregulation caused by the Q331K mutation⁵². To investigate the role of TMEM106B in TDP-43 pathology, we crossed TDP-43^{Q331K} mice with *Tmem106b*^{−/−} mice to determine how TMEM106B loss affects TDP-43 proteinopathy in the sensitized background. We first determined the effect of TMEM106B deficiency on TDP-43 homeostasis in the TDP-43^{Q331K} mice. We failed to detect cytoplasmic TDP-43 accumulation in neurons in the cortex region of *Tmem106b*^{−/−}, TDP-43^{Q331K/Q331K}, or TDP-43^{Q331K/Q331K} *Tmem106b*^{−/−} mice even when they were aged to 16-month-old (Supplementary Fig. 1a), suggesting TMEM106B loss does not lead to the cytoplasmic mislocalization of TDP-43 in TDP-43^{Q331K/Q331K} mice. Since TDP-43 turnover can be mediated by the autophagy-lysosome pathways⁵³, TMEM106B might regulate TDP-43 turnover via lysosome. To test this, we measured the total TDP-43 levels in the 16.0-month-old mouse brain cortex. TDP-43 total levels and solubility are similar in TDP-43^{Q331K/Q331K} mice with or without TMEM106B expression (Supplementary Fig. 1b, c). TDP-43^{Q331K} has been shown to cause alterations in RNA splicing⁵². To determine whether TDP-43 function is affected by TMEM106B loss, we performed RNA-seq analysis. However, we failed to detect any significant changes in gene expression in the cortex samples from TDP-43^{Q331K/Q331K} mice (Supplementary Fig. 2a and Supplementary Data 1). Additionally, previous study has demonstrated that TDP-43 Q331K mutation leads to decreased inclusion of *Sort1* exon 17b and increased inclusion of *Mapt* exons 2 and 3, as well as the generation of a mutant-specific *Sqstm1* variant that contains a truncated 7th exon and a 2 bp frameshift in exon 8⁵². However, no significant alterations were observed in any of these splicing events in TDP-43^{Q331K/Q331K}, *Tmem106b*^{−/−} or TDP-43^{Q331K/Q331K} *Tmem106b*^{−/−} mouse cortex samples (Supplementary Fig. 3). TMEM106B loss leads to significant changes in gene expression related to myelination process and lipid metabolism as previously reported⁵⁴ (Supplementary Fig. 2). TDP-43^{Q331K/Q331K} *Tmem106b*^{−/−} mice do not show any further alterations in gene expression compared to *Tmem106b*^{−/−} mice (Supplementary Fig. 2a). Collectively, these results suggest that TMEM106B loss does not trigger any obvious TDP-43 pathology or alterations in TDP-43 function in the brain of TDP-43^{Q331K} mice.

TMEM106B deficiency causes glial activation and Purkinje cell loss in TDP-43^{Q331K} mice

Next, we examined glia activation in TDP-43^{Q331K/Q331K} *Tmem106b*^{−/−} mice and found increased levels of microglia marker IBA1, activated microglia marker CD68, and astrocyte marker GFAP in the visual cortex in 10.0-month-old and 16.0-month-old TDP-43^{Q331K/Q331K} *Tmem106b*^{−/−} mice compared to aged-matched TDP-43^{Q331K/Q331K} and *Tmem106b*^{−/−} mice (Fig. 1a, b). However, no neuronal loss was found in the cortex of TDP-43^{Q331K/Q331K} *Tmem106b*^{−/−} mice (Fig. 1c, d). Previous studies have shown that TMEM106B deficiency causes Purkinje cell death specifically in the anterior lobe of the cerebellum^{41,44,45}. This phenotype is exacerbated in TDP-43^{Q331K/Q331K} *Tmem106b*^{−/−} mice, demonstrated by the increased loss of calbindin-positive cells in the anterior lobe of the cerebellum (Fig. 1e, f). In addition, elevated glial activation was found in the cerebellum (Fig. 1e, f). Taken together, our data support that TMEM106B deficiency enhances glial activation and brain pathologies in TDP-43^{Q331K/Q331K} mice without any obvious TDP-43 pathology.

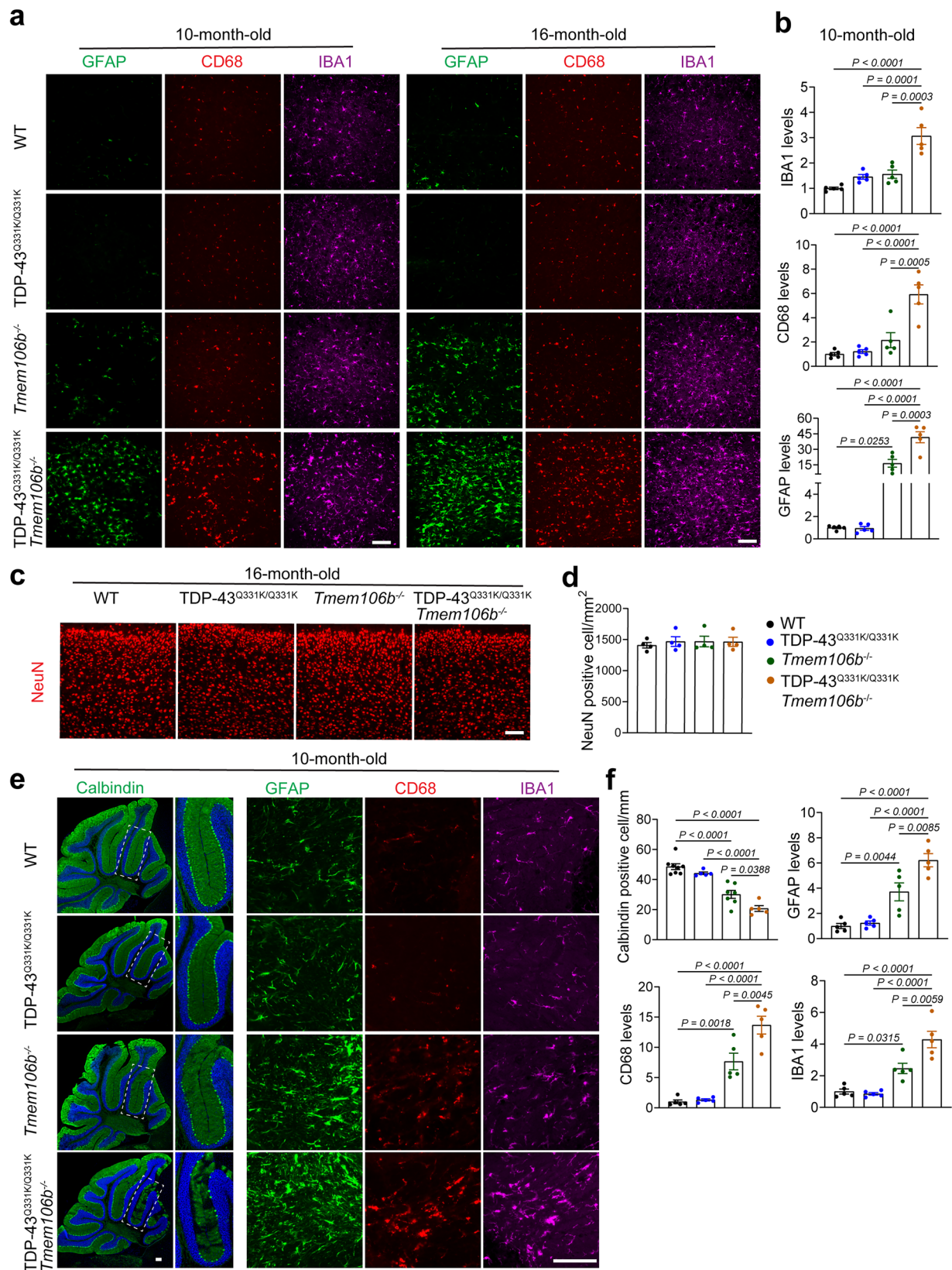
Loss of TMEM106B leads to impaired motor function in TDP-43^{Q331K} mice

TDP-43^{Q331K} mice display FTLD-like cognitive dysfunction, including executive and memory impairment, but do not develop significant motor impairments⁵². To determine the effect of TMEM106B on the motor function in TDP-43^{Q331K} mice, open field tests were performed to assess the locomotor activity of 10.0-month-old TDP-43^{Q331K/Q331K} *Tmem106b*^{−/−} and TDP-43^{Q331K/+} *Tmem106b*^{−/−} mice. We failed to observe significant differences in total distance traveled between all tested groups of mice (Fig. 2a, b), suggesting the locomotor activity is not affected by TMEM106B ablation in TDP-43^{Q331K} mice. However, TDP-43^{Q331K/Q331K} *Tmem106b*^{−/−} and TDP-43^{Q331K/+} *Tmem106b*^{−/−} mice spend more time crossing the beam compared with WT mice in the balance beam tests, indicating an impairment in motor coordination, which has been reported in TMEM106B-deficient mice previously^{41,44,45} (Fig. 2c). This is consistent with increased loss of Purkinje neurons in these mice (Fig. 1e, f). In addition, these mice display an abnormal hindlimb clasping behavior (Fig. 2d, e). In parallel with motor function studies, the cognitive defects were assessed by novel object recognition tests and Y-maze tests. TDP-43^{Q331K/Q331K} *Tmem106b*^{−/−} and TDP-43^{Q331K/+} *Tmem106b*^{−/−} mice exhibit a reduction in novelty preference similar to TDP-43^{Q331K/Q331K}, TDP-43^{Q331K/+} and *Tmem106b*^{−/−} mice when compared to WT mice (Fig. 2f). However, TDP-43^{Q331K/Q331K} *Tmem106b*^{−/−} and TDP-43^{Q331K/+} *Tmem106b*^{−/−} mice do not show any significant changes in alternation in the Y-maze tests, suggesting that spatial working memory is not influenced in these mice (Fig. 2g, h).

TMEM106B ablation leads to increased levels of cholesterol esters and proteins involved in lipid metabolism in the cerebellum of TDP-43^{Q331K} mice

Dysregulated lipid metabolism has been associated with cerebellar degeneration^{55,56}. We have found that loss of TMEM106B leads to Purkinje cell loss and elevated glial activation in TDP-43^{Q331K/Q331K} mice (Fig. 1e). Given the previously reported role of TMEM106B in lipid metabolism in brain^{57,58}, we asked whether the cerebellar pathologies in TMEM106B-deficient TDP-43^{Q331K} mice is related to the dysregulated lipid metabolism. The untargeted lipidomic analysis of 10-month-old mouse cerebellum identified 725 species within 44 lipid classes (Fig. 3a and Supplementary Data. 2). The levels of cholesterol esters (CEs) were found to be significantly upregulated in *Tmem106b*^{−/−} mice and further increased in TDP-43^{Q331K/Q331K} *Tmem106b*^{−/−} mice without statistical significance (Fig. 3b, c). The levels of several species of diglycerides (DGs) and phosphatidylcholine PC (42:8) were significantly decreased in TDP-43^{Q331K/Q331K} *Tmem106b*^{−/−} mice while the total levels of DGs and PCs were unchanged (Fig. 3b, c). Other identified lipids are not obviously affected by TMEM106B deficiency or TDP-43 Q331K mutation (Supplementary Data. 2).

To better understand molecular mechanisms underlying the cerebellum pathologies in the TDP-43^{Q331K/Q331K} *Tmem106b*^{−/−} mice, we performed proteomics analysis of cerebellar lysates from WT, TDP-43^{Q331K/Q331K}, *Tmem106b*^{−/−} and TDP-43^{Q331K/Q331K} *Tmem106b*^{−/−} mice. There are only 13 proteins showing level changes (4 upregulated and 9 downregulated) in TDP-43^{Q331K/Q331K} mice compared to 29 upregulated and 20 downregulated proteins in *Tmem106b*^{−/−} mice (absolute log2FC > 0.5, FDR < 0.05) (Fig. 3d, e and Supplementary Data. 3). Among the downregulated proteins in the TDP-43^{Q331K/Q331K} mice, the extracellular matrix protein tenascin C (TNC), playing an important role in neuronal plasticity in cerebellum^{59,60}, is also significantly decreased in *Tmem106b*^{−/−} and TDP-43^{Q331K/Q331K} *Tmem106b*^{−/−} mice (Fig. 3e, f), which might be associated with the Purkinje cell loss in cerebellum. TDP-43^{Q331K/Q331K} *Tmem106b*^{−/−} mice show more alterations in protein levels with 46 proteins upregulated and 20 downregulated compared to WT (Fig. 3d–f and Supplementary Data. 3). Many of these proteins function in the lysosomal and inflammatory pathways and were also significantly affected by TMEM106B deficiency alone (Fig. 3d–f), reflecting the changes in lysosomal activity and inflammation



caused by TMEM106B loss in the cerebellum. In addition, several proteins involved in the metabolism of glycosphingolipids, phospholipids, cholesterol, and triglycerides, such as ARSG, STARD5, HEXA, HEXB, APOE, PLD3, and BDH2 were significantly upregulated by TMEM106B ablation (Fig. 3f), suggesting that lipid metabolism in cerebellum is altered by

TMEM106B loss. Moreover, consistent with the Purkinje cell degeneration in cerebellum, TMEM106B loss leads to increased levels of the apoptotic marker CASP3 (caspase-3) and decreased levels of several proteins critical for Purkinje cell health and cerebellar functions (Fig. 3f), such as CA8 (carbonic anhydrase 8), PRKCγ (protein kinase C gamma) and CALB1

Fig. 1 | TDP-43^{Q331K/Q331K} *Tmem106b*^{-/-} mice show elevated gliosis and Purkinje cell loss. **a, b** TMEM106B deficiency leads to glia activation in TDP-43^{Q331K} mice. Immunostaining of GFAP, CD68, and IBA1 in brain sections from 10 to 16-month-old mice. Representative images from the cortex were shown. Scale bar, 100 μ m. Quantification of GFAP, CD68, and IBA1 levels from 10.0-month-old mice sections was shown in **(b)**. Data are presented as mean \pm SEM from five mice per group ($n = 5$). P values were determined using one-way ANOVA with Bonferroni's multiple comparisons and were shown on the top of the graphs. **c, d** No neuronal loss was observed in the cortex of TDP-43^{Q331K/Q331K} *Tmem106b*^{-/-} mice. Immunostaining of NeuN in brain sections from 16-month-old mice. Representative images from the

cortex were shown. Scale bar, 100 μ m. The numbers of the NeuN-positive cells/mm² in the cortex region were quantified **(d)**. Data are presented as mean \pm SEM from 4 mice per group ($n = 4$). **e, f** Exacerbated Purkinje cell loss and glial activation in TDP-43^{Q331K/Q331K} *Tmem106b*^{-/-} mice. Immunostaining of calbindin, GFAP, CD68, and IBA1 in brain sections from 10-month-old mice. Representative images from the cerebellum were shown. Scale bar, 100 μ m. The numbers of the calbindin-positive cells/mm in the cerebellum anterior lobe and GFAP, CD68, and IBA1 levels in deep cerebellar nuclei in 10.0-month-old mice were quantified **(f)**. Data are presented as mean \pm SEM from 5 to 8 mice per group ($n = 5-8$). One-way ANOVA tests with Bonferroni's multiple comparisons.

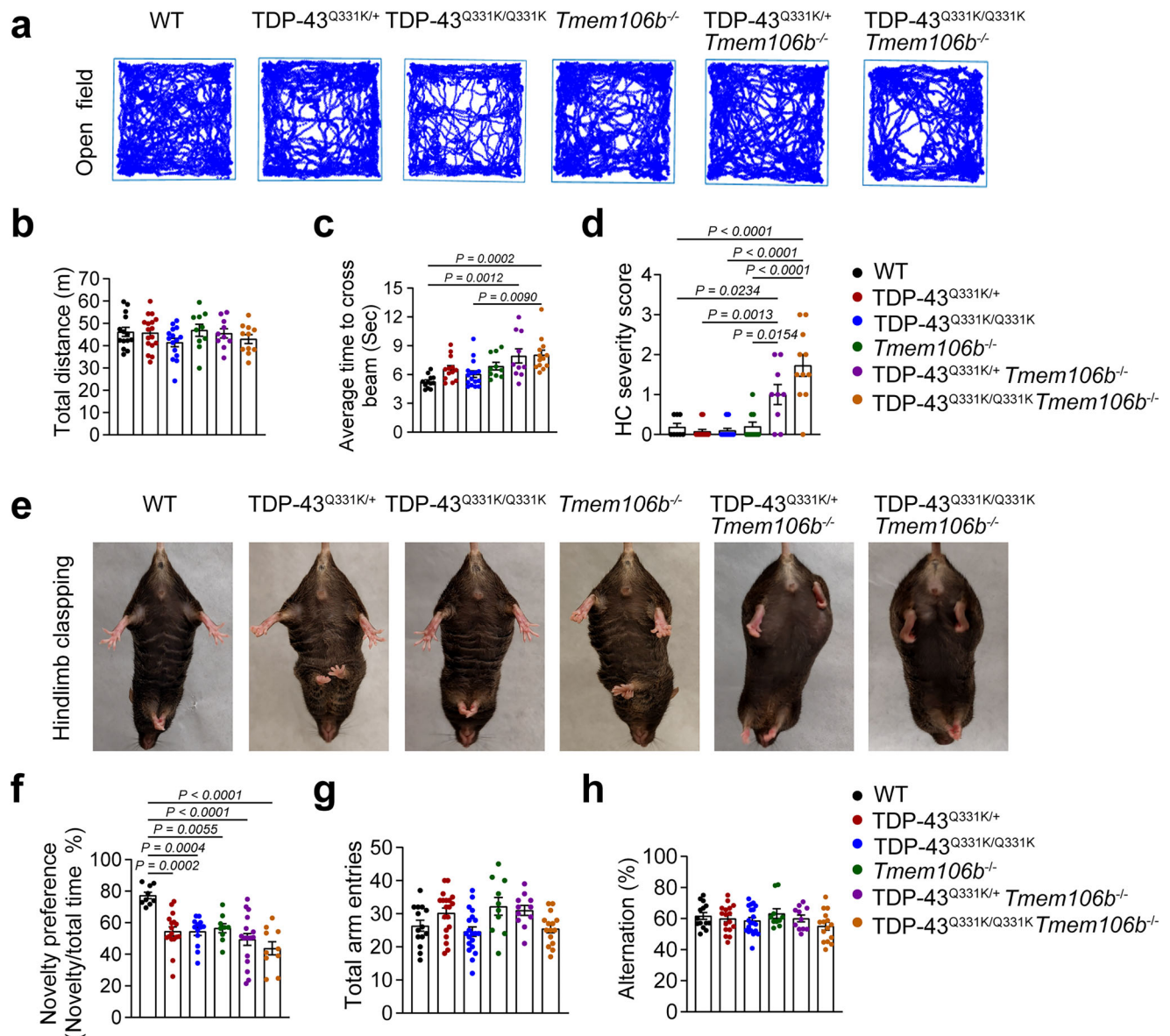
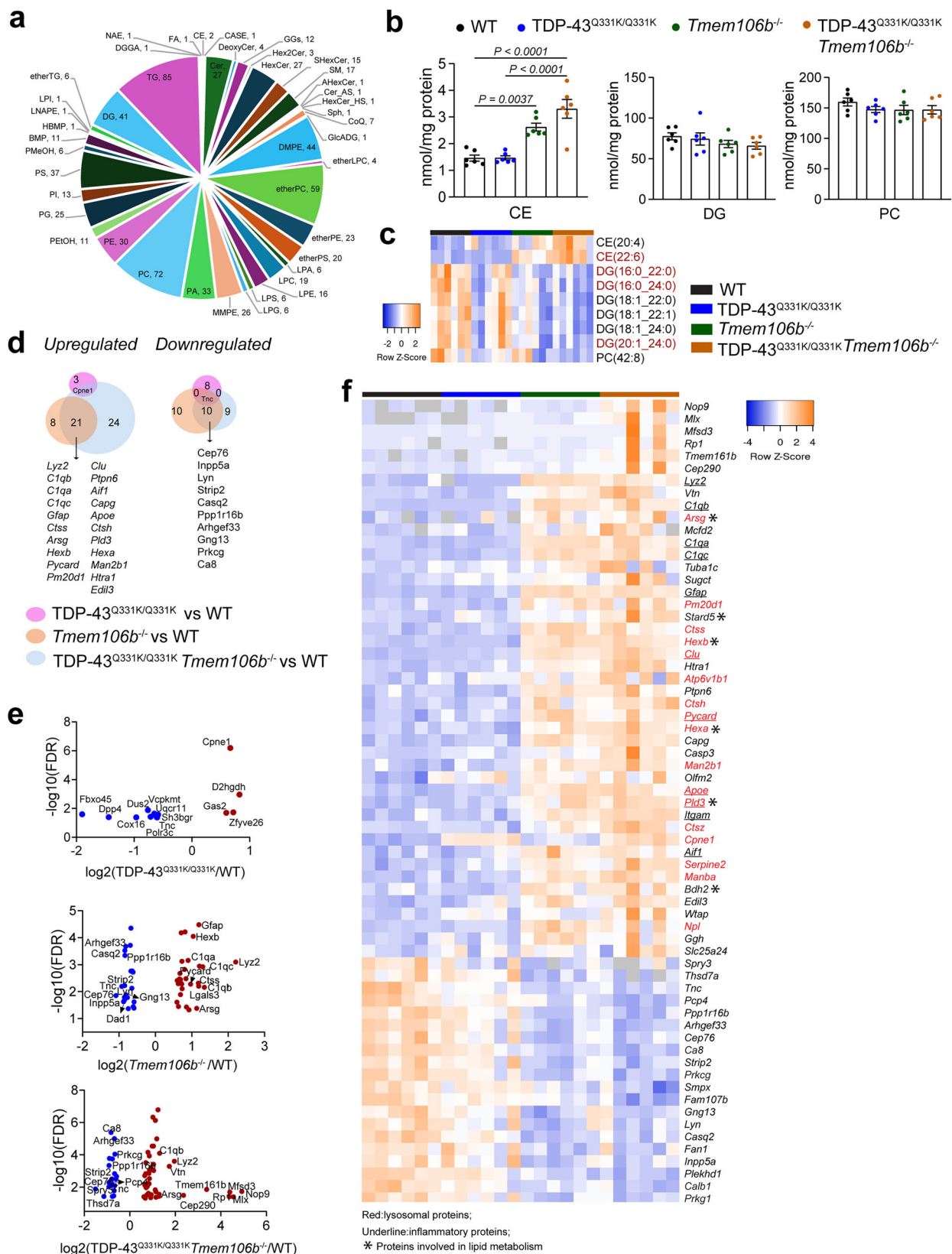


Fig. 2 | Behavioral deficits in TMEM106B-deficient TDP-43^{Q331K} mice. **a, b** The open field test was performed on 10-month-old male mice. The total distance the mice traveled was quantified. Data are presented as means of \pm SEM ($n = 10-17$ mice per genotype). One-way ANOVA tests. **c** Ten-month-old male mice were subjected to balance beam tests. The average time across the beam was shown. Data are presented as means of \pm SEM ($n = 10-16$ mice per genotype). P values were determined using one-way ANOVA tests with Bonferroni's multiple comparisons and were shown on the top of the graphs. **d, e** Hindlimb clasping behavior in 10-month-

old male mice. The severity score of hindlimb clasping (HC) was shown **(d)**. Data are presented as means of \pm SEM ($n = 8-15$ mice per genotype). One-way ANOVA tests. **f** Novel object recognition tests. Novelty preference (exploration time of the novel object/exploration time of both objects $\times 100\%$) was shown. Data are presented as means of \pm SEM ($n = 9-17$ mice per genotype). One-way ANOVA tests with Bonferroni's multiple comparisons. **g** Y-maze tests total arm entries **(g)** and alternation **(h)** were shown. Data are presented as means of \pm SEM ($n = 10-20$ mice per genotype). One-way ANOVA tests with Bonferroni's multiple comparisons.



(calbindin 1)^{61,62}. In fact, loss of CA8 and PRKCγ has been shown to cause cerebellar ataxia^{63–66}. Taken together, our lipidomic and proteomic analysis support the important role of TMEM106B in lipid metabolism and cerebellar homeostasis.

TMEM106B-deficient TDP-43^{Q331K} mice develop obesity

It has been reported that TDP-43^{Q331K} mice gain body weight due to hyperphagia⁵². Consistently, we found that the body weight of TDP-43^{Q331K/+} and TDP-43^{Q331K/Q331K} mice were significantly increased compared to

Fig. 3 | Lipid and protein changes in the cerebellum in TDP-43^{Q331K/Q331K} *Tmem106b*^{-/-} mice. Total lipids were extracted from cerebellums of 10.0-month-old WT, TDP-43^{Q331K/Q331K}, *Tmem106b*^{-/-}, TDP-43^{Q331K/Q331K} *Tmem106b*^{-/-} male mice, and lipids were analyzed by mass spectrometry ($n = 6$ mice per genotype). **a** Lipid classes identified in the cerebellum and the number of species identified in each lipid class. **b** Total levels (sum of all species) of the cholesterol esters (CE), diglycerides (DG), and phosphatidylcholines (PC) in the cerebellum. Data are presented as mean \pm SEM ($n = 6$ mice per genotype). *P* values were determined using one-way ANOVA tests with Bonferroni's multiple comparisons and were shown on the top of the graphs. **c** Heatmap was shown for the significantly changed lipid species with FDR < 0.05 and absolute log₂(FC) > 0.5 in the TDP-43^{Q331K/Q331K} *Tmem106b*^{-/-} mice

compared to the WT. Red highlighted species were also significantly altered in *Tmem106b*^{-/-} mice compared to WT. **d** Venn diagram showing the overlap of the upregulated and downregulated proteins between the indicated comparisons. **e** Volcano plots were shown for the significant changed proteins with FDR < 0.05 and absolute log₂(FC) > 0.5 in the indicated comparisons. The names of the top 10 upregulated and downregulated proteins were displayed. **f** Heatmap illustrating the changes of the proteins that significantly affected the TDP-43^{Q331K/Q331K} *Tmem106b*^{-/-} cerebellum compared to the WT (FDR < 0.05 and absolute log₂(FC) > 0.5). Only proteins with an intensity above 1000 are plotted in the heatmap. Red highlights the lysosomal proteins. Underlined text indicates the proteins involved in inflammation. Asterisks mark the proteins associated with lipid metabolism.

age-matched WT mice (Fig. 4a, b). Unexpectedly and interestingly, TMEM106B deficiency leads to a much more significant weight gain in the TDP-43^{Q331K/Q331K} and TDP-43^{Q331K/Q331K} *Tmem106b*^{-/-} mice (Fig. 4a, b). To determine whether these mice gained body weight due to increased food consumption, the daily food intake was monitored but we failed to see a significant difference between mice of different genotypes (Fig. 4c). Additionally, TDP-43^{Q331K/Q331K} *Tmem106b*^{-/-} mice show a significant enlargement of the liver, gonadal white adipose tissue (gWAT), subcutaneous white adipose tissue (sWAT), and interscapular brown fat tissue (iBAT) compared to a moderate increase of the liver and gWAT in TDP-43^{Q331K/Q331K} mice (Fig. 4d, e). Hematoxylin and eosin (H&E) staining and immunostaining of the lipid droplet (LD) marker perilipin2 showed a significant accumulation of lipid droplets in the liver and adipose tissues in TDP-43^{Q331K/Q331K} *Tmem106b*^{-/-} mice as well as increased infiltration of inflammatory cells (Fig. 4f, g). These results suggest that ablation of TMEM106B exacerbates obesity phenotypes in TDP-43^{Q331K} mice. TDP-43 is known to regulate the expression of the genes involved in lipid metabolism⁶⁷. We asked whether TMEM106B could affect TDP-43 protein homeostasis in the liver and adipose tissue, thereby leading to the dysregulation of lipid metabolism and thus the obesity phenotype. Western blot analysis showed that TDP-43 levels are barely changed by TMEM106B loss in the peripheral tissues in TDP-43^{Q331K/Q331K} mice (Fig. 5a–d) and immunostaining showed TDP-43 remains localized in the nucleus in the liver of TDP-43^{Q331K/Q331K} *Tmem106b*^{-/-} mice (Fig. 5e), suggesting that TMEM106B deficiency likely causes obesity without affecting TDP-43 protein levels or localization.

Hepatic lipid metabolism is altered by TDP-43 Q331K and TMEM106B ablation

Next, we performed lipidomic analysis to identify alterations in hepatic lipids caused by the TDP-43 Q331K mutation and TMEM106B deficiency. The untargeted lipidomic analysis identified 743 lipid species within 21 classes (Fig. 6a and Supplementary Data 4) and a dramatic change in triglycerides (TGs) levels. The levels of total triglycerides (TGs) and many TG species are significantly increased in TDP-43^{Q331K/Q331K} mouse liver samples and only 4 TG species are significantly increased in *Tmem106b*^{-/-} mouse liver (Fig. 6b, c and Supplementary Data 4). Changes in the hepatic triglyceride (TG) profile have been associated with several metabolic diseases, such as insulin resistance and metabolic-associated fatty liver diseases⁶⁸. Further analysis of the acyl chain length and saturation profile illustrated that the majority of the upregulated TGs in TDP-43^{Q331K/Q331K} mice are long-chain or very long-chain unsaturated TGs, and all 4 upregulated TGs in *Tmem106b*^{-/-} mice are long-chain unsaturated TGs (Fig. 6e). A further significant increase in TG levels is observed in TDP-43^{Q331K/Q331K} *Tmem106b*^{-/-} mouse liver (Fig. 6b), with many more long-chain and very long-chain polyunsaturated TGs involved (Fig. 6c–e). In addition, a few DGs are upregulated in TDP-43^{Q331K/Q331K} or *Tmem106b*^{-/-} mouse liver, and more DG species get significantly upregulated in TDP-43^{Q331K/Q331K} *Tmem106b*^{-/-} mice (Fig. 6b–d). Furthermore, while the total levels of phospholipids, including phosphatidylethanolamine (PE), PC, methyl phosphatidylcholine (MePC), phosphatidylglycerol (PG), phosphatidylinositol (PI) and phosphatidylserine (PS), are minimally affected

by TDP-43^{Q331K} mutation or TMEM106B deficiency, the levels of some specific PE, PC or MePC species are significantly changed in *Tmem106b*^{-/-} mice, which is further enhanced in TDP-43^{Q331K/Q331K} *Tmem106b*^{-/-} mice (Fig. 6f–h). Additionally, the levels of several species of PG, PI, or PS are either increased or decreased in *Tmem106b*^{-/-} mice or TDP-43^{Q331K/Q331K} *Tmem106b*^{-/-} mice (Fig. 6f, g). Interestingly, the levels of cardiolipin, the phospholipid component of the inner mitochondrial membrane, are significantly decreased in the liver of TDP-43^{Q331K/Q331K} *Tmem106b*^{-/-} mice (Fig. 6f, g), indicating that the mitochondrial function might be impaired in these obese mice. Moreover, there is a trend of decrease in the overall abundance of sphingomyelin in TDP-43^{Q331K/Q331K} *Tmem106b*^{-/-} mice (Fig. 6f, g), while ceramides (Cer) and hexosylceramides (Hex-Cer) are increased in the TDP-43^{Q331K/Q331K} *Tmem106b*^{-/-} mice compared to the WT (Fig. 6f, g). The level of coenzyme Q10 [Co(Q10)] is significantly increased in TDP-43^{Q331K/Q331K} *Tmem106b*^{-/-} mice (Fig. 6f, g). TMEM106B deficiency and/or TDP-43^{Q331K/Q331K} do not cause any significant changes in the total levels or specific species of other detected lipid classes (Supplementary Fig. 4). Collectively, the alterations in the lipid composition and content in the liver suggest that hepatic lipid homeostasis is disrupted by TMEM106B deficiency in the TDP-43^{Q331K/Q331K} background.

To better understand the role of TDP-43 and TMEM106B in lipid metabolism, we performed RNA-seq analysis. Transcriptome analysis identified 99 upregulated and 71 downregulated genes in TDP-43^{Q331K/Q331K} mouse liver compared with WT as well as 183 upregulated and 121 downregulated genes in *Tmem106b*^{-/-} compared with WT (Fig. 7a and Supplementary Data 5). The gene expression alterations are further exacerbated in TDP-43^{Q331K/Q331K} *Tmem106b*^{-/-} mouse liver with 517 upregulated and 310 downregulated genes compared with WT (Fig. 7a and Supplementary Data 5). Comparison of the differential expressed genes (DEGs) (absolute log₂FC \geq 0.5) revealed that genes affected by TDP-43 Q331K mutation and TMEM106B deficiency are largely non-overlapping (Fig. 7a). In total, 31 upregulated and 12 downregulated genes are shared among the three groups compared with WT (Fig. 7a, b). Additionally, we found that 83 genes are significantly upregulated and 46 genes are downregulated (absolute log₂FC \geq 0.5) in TDP-43^{Q331K/Q331K} *Tmem106b*^{-/-} group compared to all other three groups (Fig. 7a). The expression changes of these DEGs with absolute log₂FC \geq 1.0 were shown in the heatmap (Fig. 7c). Pathway enrichment analysis using the hallmark gene sets showed upregulation of multiple critical pathways related to lipid metabolism, including fatty acid metabolism, adipogenesis, peroxisome, and bile acid metabolism, in TDP-43^{Q331K/Q331K}, *Tmem106b*^{-/-}, or TDP-43^{Q331K/Q331K} *Tmem106b*^{-/-} mice compared with WT (Fig. 8a). Additionally, cholesterol homeostasis, mTORC1 signaling, and oxidative phosphorylation are significantly upregulated in *Tmem106b*^{-/-} and TDP-43^{Q331K/Q331K} *Tmem106b*^{-/-} mice compared with WT (Fig. 8a). In the most upregulated pathway “fatty acid metabolism,” gene expression alteration is much more significant in TDP-43^{Q331K/Q331K} *Tmem106b*^{-/-} mice compared to that in TDP-43^{Q331K/Q331K} or *Tmem106b*^{-/-} mice (Fig. 8b). We further performed a gene ontology (GO) enrichment analysis and found that numerous biological processes associated with fatty acid, lipid, or TG metabolism are significantly upregulated

in TDP-43^{Q331K/Q331K} *Tmem106b*^{-/-} mice compared with WT (Fig. 8c). Among them, the processes of fatty acid beta-oxidation, fatty acid metabolism, fatty acid transmembrane transport and long-chain fatty acid metabolism are also upregulated in TDP-43^{Q331K/Q331K} and *Tmem106b*^{-/-} mice compared to WT (Fig. 8c). Taken together, our lipidomic and

transcriptome analysis demonstrated that the lipid metabolism is misregulated by TDP-43 Q331K mutation and TMEM106B loss in the mice, suggesting a potential role of both TMEM106B and TDP-43 in lipid metabolism and reflecting the fatty liver phenotype in the TDP-43^{Q331K/Q331K} *Tmem106b*^{-/-} mice.

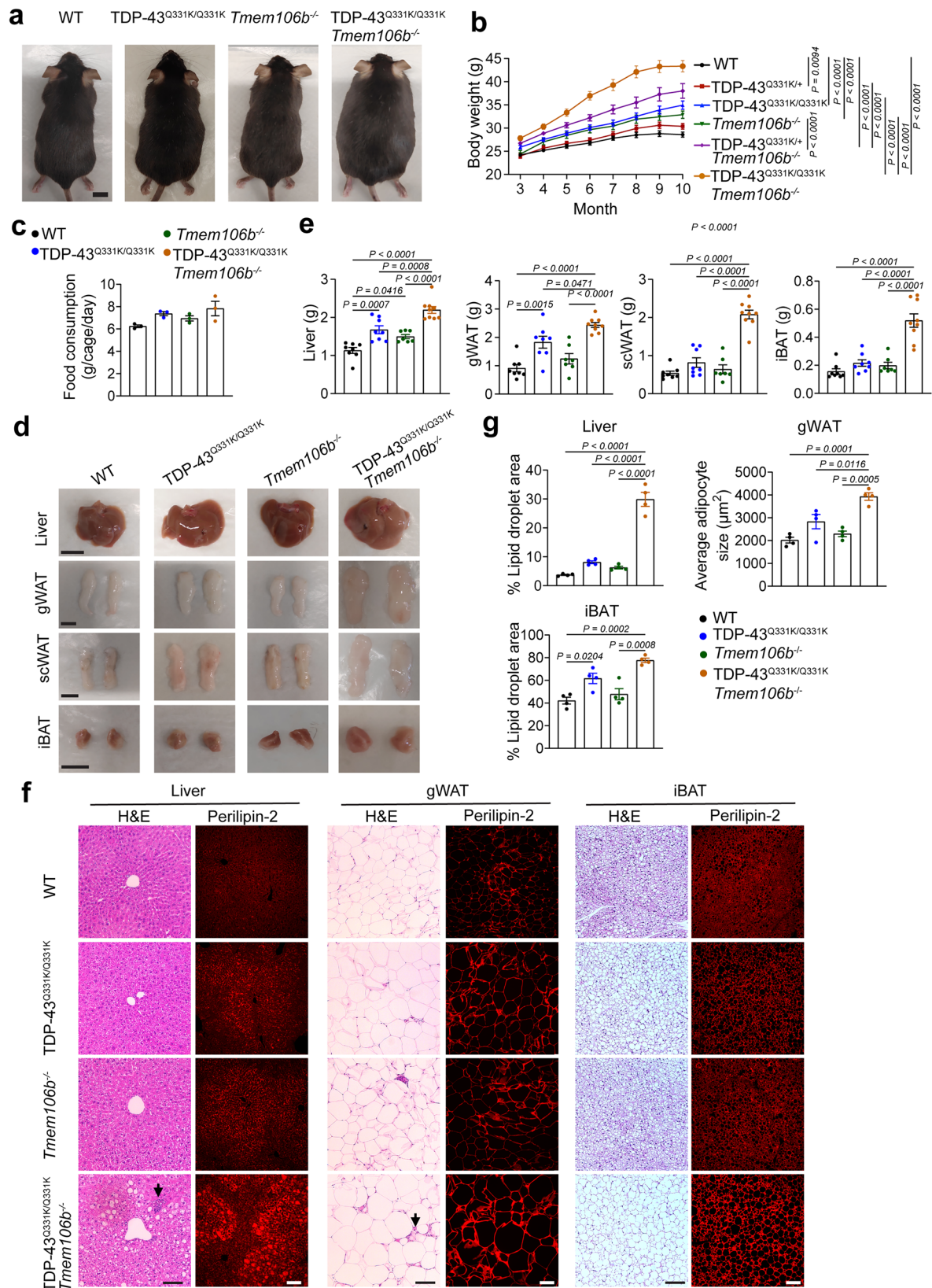


Fig. 4 | TDP-43^{Q331K} *Tmem106b*^{-/-} mice develop obesity. **a** Representative images of 10-month-old WT, TDP-43^{Q331K/Q331K}, *Tmem106b*^{-/-}, TDP-43^{Q331K/Q331K}*Tmem106b*^{-/-} male mice. Scale bar, 1 cm. **b** Body weight of 10-month-old male mice of the indicated genotypes was measured and analyzed. Data are presented as mean ± SEM (*n* = 11–22 mice per genotype). *P* values were determined using two-way ANOVA tests with repeated measures. **c** Daily food consumption of 9-month-old male mice over 2 weeks. Data are presented as mean ± SEM (*n* = 3 cages per genotype). One-way ANOVA tests. **d** Representative images of the liver, gonadal white adipose tissues (gWAT), subcutaneous white adipose tissues (sWAT), and interscapular brown adipose tissue (iBAT) of 10-month-old male mice of the indicated genotypes. Scale bar, 1 cm. **e** The

weight of the indicated peripheral tissues of 10-month-old male mice of the indicated genotypes. Data are presented as mean ± SEM (*n* = 7–9 mice per genotype). One-way ANOVA tests with Bonferroni's multiple comparisons. **f** H&E staining and immunostaining of lipid droplet marker perilipin2 in the liver, gonadal white adipose tissue (gWAT), and interscapular brown adipose tissue (iBAT) of 10-month-old male mice. Representative images were shown. The arrow indicates the inflammatory cell infiltration in the liver and the crown-like structures in gWAT. Scale bar, 100 μm. **g** The area of the lipid droplet in the liver and iBAT and the adipocyte size of gWAT were quantified. Data are presented as mean ± SEM (*n* = 4 mice per genotype). One-way ANOVA tests with Bonferroni's multiple comparisons.

Discussion

Both TDP-43 and TMEM106B have emerged as key players in neurodegeneration and brain aging⁶⁹. In this study, we show that TMEM106B deficiency leads to obesity in the TDP-43^{Q331K} knock-in mice and reveal novel functions of TMEM106B and TDP-43 in lipid metabolism.

Role of TMEM106B in TDP-43 proteinopathy

TMEM106B risk alleles correlated with increased TMEM106B levels have been associated with enhanced TDP-43 proteinopathy^{7,12,14–16}. However, in ALS patients the minor allele of TMEM106B, correlated with lower TMEM106B levels, was found to have more TDP-43 pathology⁴⁸. In addition, partial loss of TMEM106B was found to cause cytoplasmic aggregation of TDP-43 in cell culture⁴⁸. Thus, it remains unclear how TMEM106B affects TDP-43 pathology. TDP-43 aggregates can be cleared by macroautophagy and chaperone-mediated autophagy, both of which depend on lysosomal degradation^{53,70}. We hypothesized that lysosomal defects caused by TMEM106B dysfunction could be one of the mechanisms leading to TDP-43 aggregation. In this study, we investigate the effect of TMEM106B loss in the TDP-43^{Q331K} mice, which do not develop typical TDP-43 pathology but show perturbed TDP-43 homeostasis and function. However, TMEM106B loss does not seem to affect TDP-43 levels and distribution in the brain of TDP-43^{Q331K/Q331K} mice (Supplementary Fig. 1). We previously detected an increase in pTDP-43 levels in insoluble fractions of 16-month-old TMEM106B knockout mouse brain using an anti-pTDP-43 S403/S404 antibody (COSMO BIO, CAC-TIP-PTD-P05) compared to age-matched WT⁴⁵. However, this antibody is no longer available and we failed to detect pTDP-43 in 16-month-old TMEM106B knockout mouse brain using a different anti-pTDP-43 antibody (rabbit anti-pTDP-43 Ser409/410, Proteintech group, 80007-1-RR), which might be due to the lower sensitivity of this antibody or the absence of phosphorylation of TDP-43 at S409/410 sites in TMEM106B knockout mice. In addition, although alterations in gene splicing have been previously detected in TDP-43^{Q331K} mouse brain⁵², our RNA-seq and qRT-PCR analysis of 10.0-month-old mouse brain revealed no significant changes in gene expression and splicing in TDP-43^{Q331K/Q331K} mice and TDP-43^{Q331K/Q331K} *Tmem106b*^{-/-} mice compared with WT (Supplementary Fig. 2, Fig. 3 and Supplementary Data 1), indicating TMEM106B loss is unlikely to alter TDP-43 function. Recently, TMEM106B C-terminal fragments (CTFs) have been shown to form amyloid fibrils in neurodegenerative diseases with TDP-43 pathology^{30,34} and TMEM106B CTF fibrils are correlated with increased TDP-43 dysfunction⁴⁷. Thus, TMEM106B CTF fibril formation rather than TMEM106B loss of function may enhance TDP-43 aggregation. Additionally, since TMEM106B overexpression causes lysosomal abnormalities⁶⁹, it is also conceivable that an elevation in TMEM106B levels associated with TMEM106B risk alleles could enhance TDP-43 proteinopathy by impairing lysosomal degradation of TDP-43.

Behavioral deficits and brain pathological changes in TMEM106B-deficient TDP-43^{Q331K} mice

As demonstrated previously, TDP-43^{Q331K} mice display FTL-like cognitive dysfunction but no significant motor impairment⁵². However, TDP-43^{Q331K} *Tmem106b*^{-/-} mice develop significant motor deficits with reduced motor activities in the balance beam test and altered hindlimb clasping behavior

(Fig. 2c–e). Cerebellar dysfunction has been linked to FTL and ALS^{71–74}. We observed severe Purkinje cell degeneration accompanied by glial activation in the cerebellum of TDP-43^{Q331K/Q331K} *Tmem106b*^{-/-} mice (Fig. 1e, f), which is consistent with increased motor dysfunction in these mice (Fig. 2c–e) and a critical role of Purkinje cell in motor function⁷⁵. Previous studies have demonstrated that TMEM106B is critical for maintaining the Purkinje cells health and survival during aging^{44,76,77}. However, the mechanism underlying is unclear. Our proteomic analysis revealed increased levels of apoptotic protein CASP3 and decreased levels of several proteins important for maintaining proper cerebellar functions in TDP-43^{Q331K/Q331K} *Tmem106b*^{-/-} mice (Fig. 3f). Notably, tenascin C (TNC), a ECM molecule involved in neurogenesis and regeneration^{59,78,79}, was downregulated by both TDP-43 Q331K mutation and TMEM106B deficiency (Fig. 3e, f), which might be associated with the increased Purkinje cells loss in TDP-43^{Q331K/Q331K} *Tmem106b*^{-/-} mice. In addition, previous studies⁷⁶ and our studies have identified that the lysosomal and inflammation pathways are the most affected in the TMEM106B-deficient cerebellum (Fig. 3f), indicating the lysosomal defects and inflammation may be the key mechanisms underlying Purkinje cell loss in cerebellum. Moreover, TMEM106B deficiency leads to alterations in lipids (Fig. 3b, c), specifically the cholesterol ester accumulation, and the changes in proteins regulating lipid metabolism (Fig. 3f), suggesting a potential correlation between dysregulated lipid metabolism and the cerebellar pathologies caused by TMEM106B loss.

TDP-43 Q331K mutation and TMEM106B deficiency affect hepatic lipid metabolism via independent pathways

TDP-43 is known to be involved in fat metabolism, likely through its function in regulating the expression of genes related to lipid metabolism in periphery tissues. One of the TDP-43 targets is *Tbc1d1*, a key regulator of glucose 4 transporter (GLUT4) translocation in skeletal muscle and an obesity risk factor in humans⁸⁰. Deletion of TDP-43 reduces the mRNA expression of *Tbc1d1*, leading to fat loss in mice⁸⁰. In contrast, overexpression of TDP-43 in a TDP-43 transgenic mouse line led to elevated levels of *Tbc1d1* in skeletal muscle and increased body fat⁸¹. We found mice with TDP-43 Q331K mutation develop a mild obese phenotype (Figs. 4–6), further supporting the role of TDP-43 in fat metabolism. TDP-43 Q331K has been demonstrated to interfere with the function of TDP-43 in splicing⁸². In line with the role of TDP-43 in gene expression, our RNA-seq analysis of liver samples revealed that the expression of genes associated with lipid metabolism is significantly altered in TDP-43^{Q331K} mouse liver (Fig. 7a). However, it remains unknown whether these genes are directly targeted by TDP-43. Nonetheless, given the primary role of TDP-43 in RNA metabolism, we propose that TDP-43 Q331K-triggered gene expression changes in lipid metabolism may contribute to the obese phenotype in mice.

As a lysosomal membrane protein, how TMEM106B regulates lipid metabolism is still unclear. Our lipidomics analysis of liver samples showed that TMEM106B loss has a bigger effect on phospholipid metabolism, while TDP-43 Q331K leads to more alterations in TGs (Fig. 6). In addition, RNA-seq analysis showed that the gene expression changes caused by TMEM106B deficiency and TDP-43 Q331K mutations are largely non-overlapping (Fig. 7). Furthermore, since TDP-43 levels and cellular

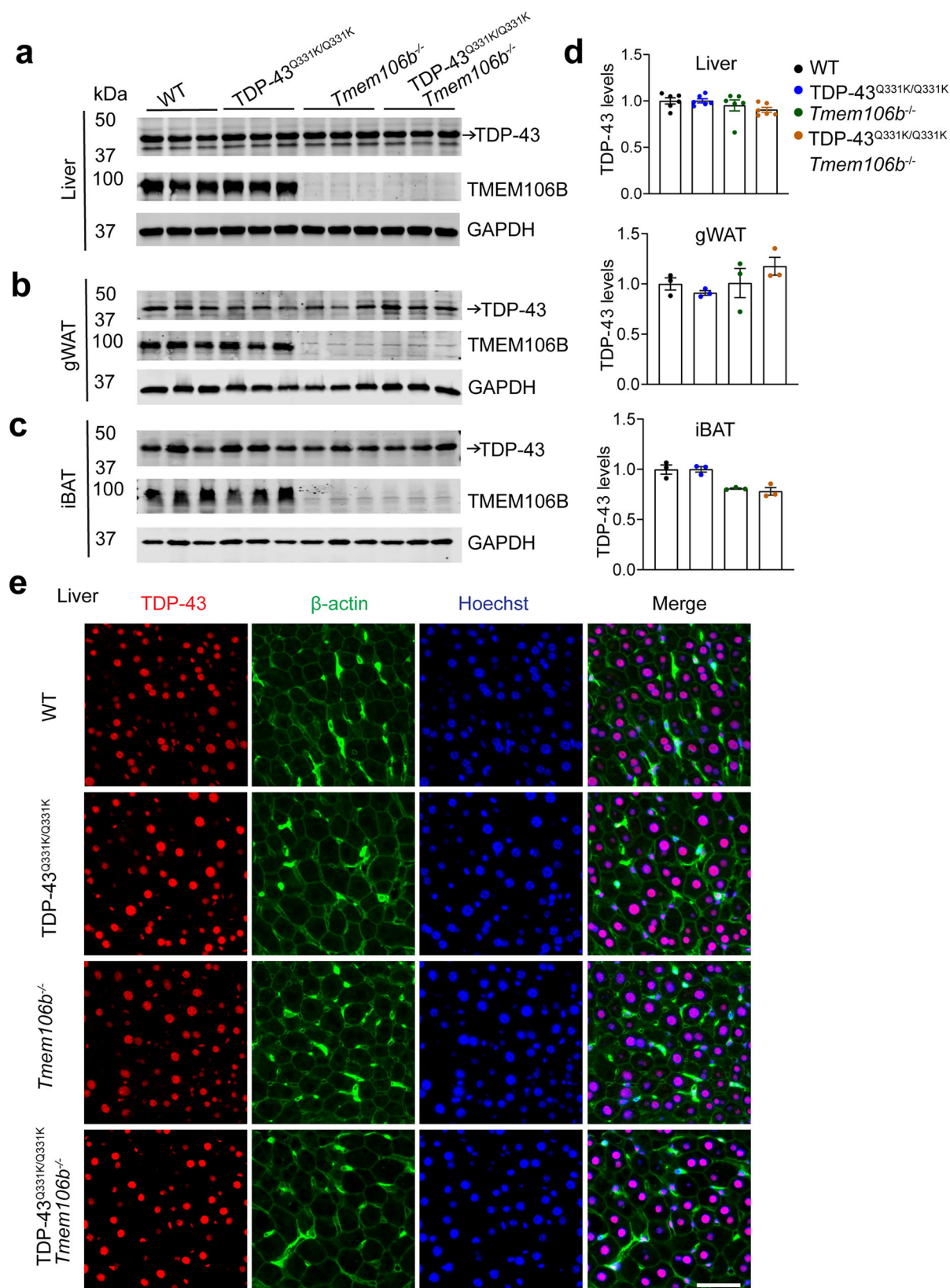
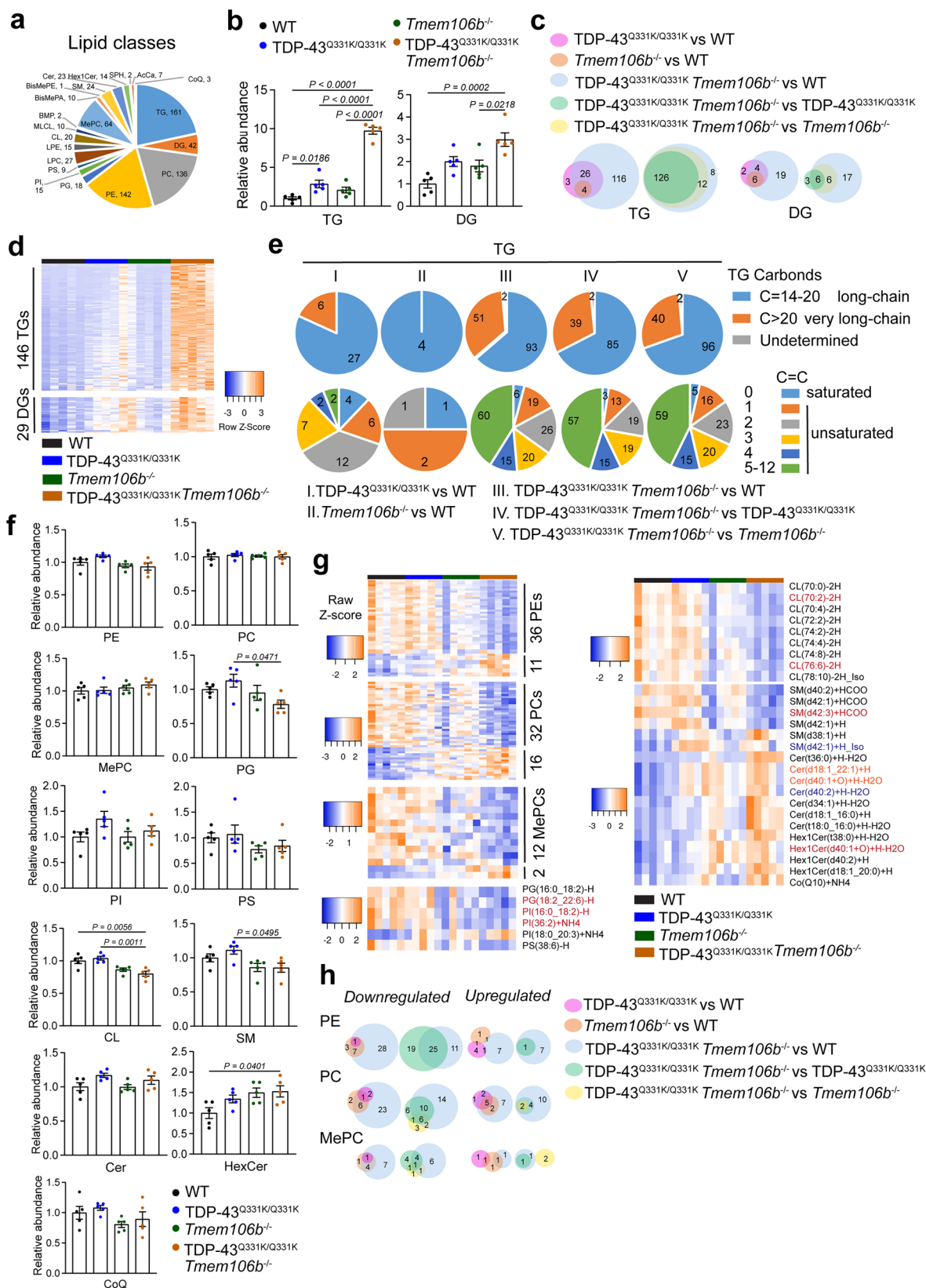


Fig. 5 | TDP-43 levels and distribution in liver and adipose tissue. Western blot analysis of TDP-43 and TMEM106B levels in the liver (a), gWAT (b), and iBAT (c) of 10-month-old WT, TDP-43^{Q331K/Q331K}, *Tmem106b*^{-/-}, TDP-43^{Q331K/Q331K} *Tmem106b*^{-/-} male mice. d TDP-43 levels were quantified and normalized to GAPDH. Data are

presented as mean ± SEM (n = 3–6 mice per genotype). e Immunostaining of TDP-43 and β-actin in liver sections from 10-month-old mice. Representative images were shown. Scale bar, 50 μm.



localization are not affected by TMEM106B loss (Fig. 5), the enhanced obesity phenotype caused by TMEM106B loss in TDP-43^{Q331K} mice is unlikely mediated by TDP-43. Taken together, these results indicate that TDP-43 and TMEM106B are likely to affect hepatic lipid metabolism via independent pathways.

Lipid metabolism and neurodegeneration

Both TMEM106B and TDP-43 are associated with a wide range of brain disorders^{1,69}, but their roles in neurodegeneration remain to be fully dissected. In this study, we provide evidence supporting the role of TMEM106B and TDP-43 in lipid metabolism. Lipids play a critical role in brain health

Fig. 6 | Alterations in lipids in the liver of TDP-43^{Q331K/Q331K} *Tmem106b*^{-/-} mice. Total lipids were extracted from 10.0-month-old male mouse liver and lipids were analyzed by mass spectrometry ($n = 5$ mice per genotype). **a** Lipid classes identified in the liver and the number of species identified in each lipid class. **b** Relative abundance of the TG and DG species in the mouse liver samples of indicated genotypes. Data are presented as mean \pm SEM ($n = 5$ mice per genotype). P values were determined using one-way ANOVA tests with Bonferroni's multiple comparisons and were shown on the top of the graphs. **c** Venn diagrams showing the overlap of the upregulated TGs identified in the indicated comparisons. **d** Heatmaps showing the significantly upregulated TG and DG species with $FDR < 0.05$ and $\log_2(FC) > 0.5$ in the TDP-43^{Q331K/Q331K} *Tmem106b*^{-/-} mouse liver compared to the WT. **e** Pie charts on top panel showing the number of long-chain and very long-chain TGs upregulated in the indicated comparisons. The TGs were divided into long-chain TGs (acyl chains ranging between 14 and 20 carbons in length), very long-chain TGs (at least one acyl chain contains carbons > 20), and the TGs with

undetermined carbons within each acyl chain. Pie charts on bottom panel showing the number of saturated (double bond = 0), monounsaturated (double bond = 1), and polyunsaturated TGs (double bond ≥ 2) upregulated in the indicated comparisons. **f** Relative abundance of PE, PC, MePC, PG, PI, PS, CL, SM, Cer, HexCer, and CoQ in the liver samples of indicated genotypes. Data are presented as mean \pm SEM ($n = 5$ mice per genotype). P values were determined using one-way ANOVA tests with Bonferroni's multiple comparisons and were shown on the top of the graphs. **g** Heatmaps were shown for the significantly changed PE, PC, MePC, PI, PG, CL, HexCer, Cer, and CoQ10 species with $FDR < 0.05$ and $\log_2(FC) > 0.5$ in TDP-43^{Q331K/Q331K} *Tmem106b*^{-/-} mice compared with WT. Blue and red highlighted species are significantly changed in TDP-43^{Q331K/Q331K} and *Tmem106b*^{-/-} mice, respectively. Orange highlighted are significantly changed in both TDP-43^{Q331K/Q331K} and *Tmem106b*^{-/-} mice. **h** Venn diagrams showing the overlap of the significantly changed PE, PC, and MePC species identified in the indicated comparisons.

and dysregulated lipid metabolism has been implicated in multiple neurodegenerative diseases, including AD^{83,84}, FTL^{85,86}, and ALS^{85,87,88}.

Several studies have suggested the role of TMEM106B in myelin lipid metabolism. A point mutation in TMEM106B causes a rare form of hypomyelinating leukodystrophy (HLD)²⁶. The myelin lipids are found to be altered in postmortem brain samples from human patients carrying the *TMEM106B* rs1990622-A dementia risk allele⁵⁸ and *TMEM106B*-deficient mouse brain⁵⁷. Furthermore, *TMEM106B*-deficient mice show myelination defects and alterations in gene expression in the myelination pathway^{42,54} (Supplementary Fig. 2). A recent study demonstrated that *TMEM106B* regulates the metabolism of galactosylceramide (GalCer) and sulfatide (ST), two major classes of myelin lipids, by influencing the activity of galactosylceramidase that hydrolyzes GalCer⁵⁷. However, changes in galactosylceramidase activity were observed in the cerebrum but not in the cerebellum under *TMEM106B* deficiency⁵⁷. In this study, we did not detect significant changes in these myelin lipids in *TMEM106B*-deficient cerebellum possibly due to technical limitations, but we did see significant changes in the levels of proteins involved in myelin lipid metabolism (Fig. 3), including the beta-hexosaminidase subunits HEXA and HEXB that mediate the GM2 ganglioside degradation⁸⁹ and arylsulfatase G (ARSG) that can catalyze the hydrolysis of sulfate esters from sulfolipids⁹⁰. In addition, we found *TMEM106B* deficiency causes cholesterol esters (CEs) accumulation in the cerebellum (Fig. 3b). Consistently, the levels of APOE, a major AD risk factor that participates in cholesterol metabolism and lipid transport⁹¹, as well as STARD5, a protein involved in cholesterol transport⁹², were found to be upregulated in *TMEM106B*-deficient cerebellum (Fig. 3b). Elevated CEs in the brain have been found in neurodegenerative diseases and might play a pathologic role under these conditions⁹³. Abnormal CE levels might be associated with Purkinje cell death in the *TMEM106B*-deficient cerebellum. Moreover, the levels of phospholipase PLD3, a recently identified lysosomal S, S-BMP synthase⁹⁴, was found to be increased upon *TMEM106B* loss. Our findings suggest that lipid metabolism is dysregulated in *TMEM106B*-deficient cerebellum, which might be a potential mechanism contributing to cerebellar degeneration associated with *TMEM106B* loss.

Previous studies have found significant alterations in lipid compositions in human patients and mouse models associated with TDP-43 misregulation. Ninety-seven percent of ALS patients develop TDP-43 pathology, and significant changes in lipid profiles have been found in patient biofluids^{67,95–97}. Lipid alterations in the human frontal cortex of ALS-FTLD patients with TDP-43 proteinopathy have also been reported⁹⁸. Whether TDP-43 dysfunction contributes to lipid metabolism abnormalities in human patients remains to be determined, however, studies using the TDP-43 deletion mice⁸⁰ and TDP-43 mouse models expressing ALS-associated mutations^{81,99,100}, including the TDP-43^{Q331K} knock-in mouse model used here, have demonstrated an important role of TDP-43 in lipid metabolism. Further studies are warranted to determine the contributions of lipid alterations caused by *TMEM106B* and TDP-43 dysfunction to neurodegeneration.

Methods

Antibodies and reagents

The following antibodies were used in this study: rabbit anti-IBA-1 (Wako, 01919741, 1:500 for immunostaining), rat anti-CD68 (Bio-Rad, MCA1957, 1:300 for immunostaining), mouse anti-NeuN (Millipore, MAB377, 1:500 for immunostaining), mouse anti-GFAP (Cell signaling, 3670S, 1:500 for immunostaining), rabbit anti-Perilipin2 (Proteintech group, 15294-1-AP, 1:300 for immunostaining), rabbit anti-calbindin (Proteintech Group, 60004-1-Ig, 1:300 for immunostaining), rabbit anti-TDP43 (Proteintech Group, 12892-1-AP, 1:500 for immunostaining and 1:5000 for western blot), rabbit anti-phospho-TDP-43 (Ser409/410) (Proteintech group, 80007-1-RR, 1:5000 for western blot), mouse anti-GAPDH (Proteintech Group, 60004-1-Ig, 1:5000 for western blot), anti- β actin (Proteintech Group, 66009-1-Ig, 1:500 for immunostaining) and rabbit anti-TMEM106B antibodies (1:1000 for western blot) were characterized previously³⁶.

The following reagents were also used in the study: Autofluorescence Quencher (Biotium, 23007), Odyssey blocking buffer (LI-COR Biosciences, 927-40000), O.C.T compound (Electron Microscopy Sciences, 62550-01).

Mouse strains

Tmem106b^{-/-} mice in C57BL/6 background were generated by our laboratory as previously described⁴⁵. TDP-43^{Q331K} mice⁵² in C57BL/6 background were obtained from the Jackson laboratory. TDP-43^{Q331K/Q331K} or TDP-43^{Q331K/Q331K} *Tmem106b*^{-/-} mice were generated by crossing TDP-43^{Q331K/Q331K} and *Tmem106b*^{-/-} mice. The male mice were used in this study due to male TDP-43^{Q331K} mice having more severe phenotypes than the female mice⁵². All the mice were housed in the Weill Hall animal facility at Cornell. Mice were euthanized by using the CO₂ or PBS perfusion according to the guidelines of animal facility. All animal procedures have been approved by the Institutional Animal Care and Use Committee (IACUC) at Cornell. We have complied with all relevant ethical regulations for animal use.

Mouse food consumption and body weight measurement

Daily food consumption was monitored for consecutive 14 days for 9-month-old WT, TDP-43^{Q331K/Q331K}, *Tmem106b*^{-/-}, TDP-43^{Q331K/Q331K} *Tmem106b*^{-/-} mice. Cages containing 2 mice of the same genotype were topped up with 200 g of food in the morning. The food left in the hopper together with any obvious food pellet in the cage was weighed the next morning. The weight of consumed food was calculated and recorded as the daily food consumed.

The body weight of WT, TDP-43^{Q331K/Q331K}, TDP-43^{Q331K/Q331K} *Tmem106b*^{-/-}, TDP-43^{Q331K/Q331K} *Tmem106b*^{-/-} and TDP-43^{Q331K/Q331K} *Tmem106b*^{-/-} mice were measured monthly. Mouse body weight was monitored for consecutive 7 months starting from 3 months old.

Behavioral test

Ten-month-old WT, TDP-43^{Q331K/Q331K}, TDP-43^{Q331K/Q331K} *Tmem106b*^{-/-}, TDP-43^{Q331K/Q331K} *Tmem106b*^{-/-} male mice (8–20 mice/group) were subject to the following behavioral tests: (1) Open-

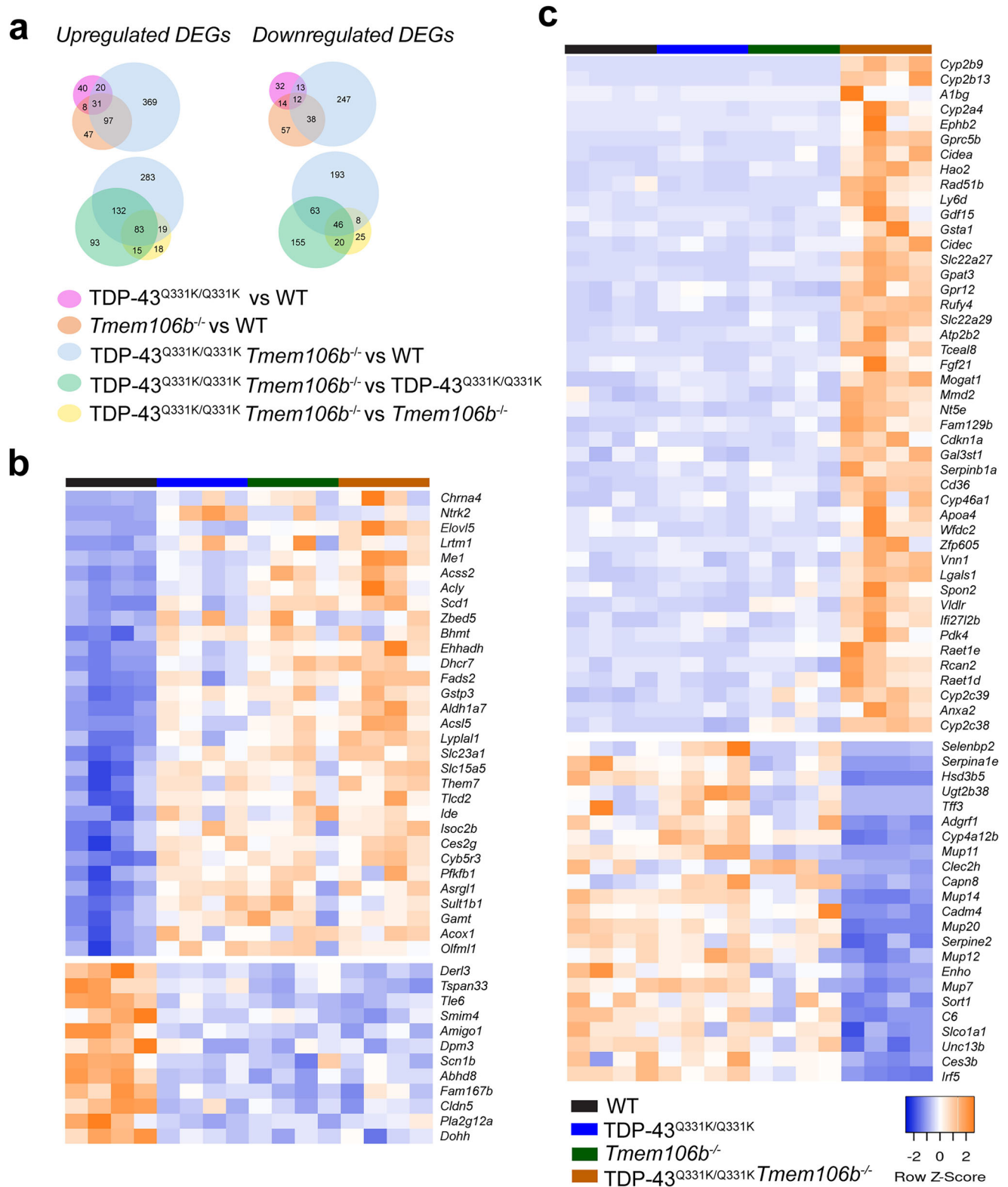


Fig. 7 | Gene expression changes in the liver of TDP-43^{Q331K/Q331K} *Tmem106b*^{-/-} mice. Total RNAs were extracted from the liver of 10-month-old male mice and the RNA-seq was performed to analyze gene expression changes ($n = 4$ mice per genotype). **a** Venn diagrams showing the overlap of the differentially expressed genes (DEGs) identified in the indicated comparisons. DEGs with $FDR \leq 0.05$ and absolute $\log_2(FC) \geq 0.5$ were

selected and analyzed. **b** Heatmap illustrating the expression changes of overlapping DEGs identified in the top Venn diagram in (a). DEGs with $FDR \leq 0.05$ and absolute $\log_2(FC) \geq 0.5$ were plotted. **c** Heatmap illustrating the expression changes of the overlapping DEGs identified in the bottom Venn diagram in (a). DEGs with $FDR \leq 0.05$ and absolute $\log_2(FC) \geq 1.0$ were plotted.

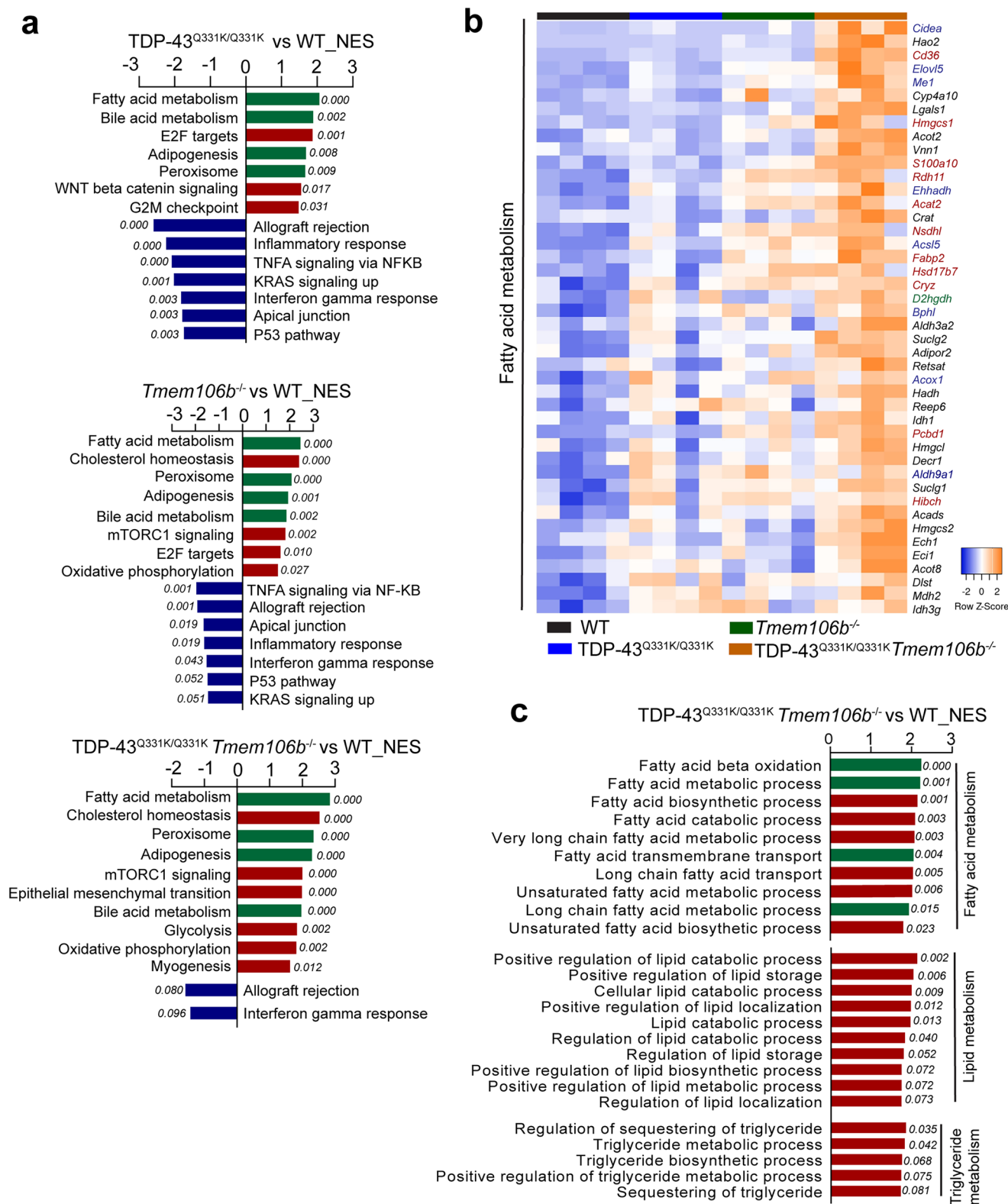


Fig. 8 | Pathways affected by TMEM106B deficiency or TDP-43^{Q331K} mutation in liver. **a** Pathway enrichment analysis was performed by GSEA using hallmark gene sets. The significantly upregulated and downregulated gene sets (FDR q -value < 0.1) in the indicated groups compared to WT are listed. The gene sets with normalized enrichment score (NES) > 1.0 are upregulated and those with NES < -1 are downregulated in the indicated groups. Green highlights the upregulated pathways shared by the indicated three comparisons. FDR q -values are listed in the bar chart. **b** Heatmap illustrating the expression changes of DEGs that contribute most to the enrichment of fatty acid metabolism pathway in TDP-43^{Q331K/Q331K}

Tmem106b^{-/-} liver samples based on GSEA results. Green and red highlighted genes were also significantly upregulated in TDP-43^{Q331K/Q331K} mice and *Tmem106b*^{-/-}, respectively, and blue highlighted were significantly upregulated in both groups. **(c)** Pathway enrichment analysis was performed by GSEA using gene sets of ontology biological process (GOBP). The pathways involved in fatty acid, lipid, and TG metabolism were significantly upregulated (FDR q value < 0.1 , NES > 1.0) in TDP-43^{Q331K/Q331K} *Tmem106b*^{-/-} liver. Green highlighted pathways were also upregulated in both TDP-43^{Q331K/Q331K} and *Tmem106b*^{-/-} mice. FDR q -values are listed in bar chart.

field test: Mice were placed in a clean plastic chamber (45 × 45 × 45 cm) for 10 min. The total distance traveled was tracked by the Viewer III software (Bioobserve, Bonn, Germany). The apparatus was thoroughly cleaned with 70% ethanol between trials. (2) Balance beam test: Beams that were 80 cm in length were used in the balance beam test for motor coordination. A bright light was used as an aversive stimulus at the start platform and an escape box (20 × 20 × 20 cm) was placed at the end of the beam. The animals were trained for 3 consecutive trials on each beam for 3 consecutive days and then were tested on the fourth day. The time taken to traverse the beam was recorded for each trial. The average time to cross the beam of the three trials was calculated. The maximum time cutoff was 60 s. (3) Hindlimb clasping test: Mice were suspended by the base of the tail and their behaviors were recorded for 30 s. Hindlimb clasping was rated from 0 to 3 based on severity¹⁰¹. (4) Y-Maze test: Spatial working memory performance was assessed by recording spontaneous alternation behavior in a Y-maze. Y-maze was made of light gray plastic and consisted of 3 arms at 120°. Each arm was 6 cm wide and 36 cm long and had 12.5 cm high walls. Each mouse was placed in the Y maze and allowed to move freely during an 8-minute session. The series of arm entries was recorded visually, and arm entry was considered to be completed when the hind paws of the mouse were completely placed in the arm. The maze was cleaned with 70% ethanol after each mouse. Alternation was defined as successive entries into the 3 arms on overlapping triplet sets (e.g., ABC, BCA). The percentage of alternation was calculated as the ratio of actual to possible alternations (defined as the total number of arm entries minus two). (5) Novel object recognition test: Mice were first exposed to two identical objects for 10 min, followed by a 2 h retention interval, and then put back into the same chamber where a novel object was introduced and monitored for 3 min. Exploration, defined as any type of physical contact with an object (whisking, sniffing, rearing on, or touching the object), was recorded and analyzed using the tracing software Viewer III. The preference score (%) for the novel object was calculated as (exploration time of the novel object/exploration time of both objects) × 100%. For all behavioral analyses, experimenters were blind to the genotypes of the mice.

Tissue lysate preparation

Mice were anaesthetized using isoflurane. Mice were then perfused with cold PBS and tissues were dissected and snap-frozen with liquid nitrogen and kept at −80 °C. On the day of the experiment, frozen tissues were thawed and homogenized on ice with bead homogenizer (Moni International) in ice-cold RIPA buffer (150 mM NaCl, 50 mM Tris-HCl [pH 8.0], 1% Triton X-100, 0.5% sodium deoxycholate, 0.1% SDS) with 1 mM PMSF, and 1× protease inhibitors (Roche). After centrifugation at 14,000 × g for 15 min at 4 °C, supernatants were collected for analysis. The insoluble pellets were washed with RIPA buffer and extracted in 2× v/w of Urea buffer (7 M Urea, 2 M Thiourea, 4% CHAPS, 30 mM Tris, pH 8.5). After sonication, samples were centrifuged at 200,000 × g at 24 °C for 1 h and the supernatant was collected as the urea-soluble fraction.

Immunofluorescence staining, H&E staining, image acquisition, and analysis

For mouse brain section staining, mice were perfused with cold PBS, and tissues were post-fixed with 4% paraformaldehyde (PFA). After dehydration in 30% sucrose buffer, tissues were embedded in the O.C.T. compound. Brain sections with 18-μm-thickness were cut with cryotome. Antigen retrieval was performed by microwaving in citrate buffer (pH 6.0) for 15 min. Tissue sections were blocked and permeabilized with 0.1% saponin in Odyssey blocking buffer before incubating with primary antibodies overnight at 4 °C. The next day, sections were washed 4 times with PBS followed by incubation with secondary fluorescent antibodies and Hoechst at room temperature for 2 h. The sections were treated with the Auto-fluorescence Quencher (TRUE Black) to quench the autofluorescence. The slides were then mounted using a mounting medium (Vector Laboratories). Images were acquired on a CSU-X spinning disc confocal microscope (Intelligent Imaging Innovations) with an HQ2 CCD camera

(Photometrics) using 40× or 63× objectives. Lower magnification images were captured by 10× or 20× objectives on a Leica DMi8 inverted microscope.

For the quantitative analysis of GFAP, CD68, and IBA1 levels in the brain sections, the fluorescence intensity was measured using ImageJ after a threshold application. To quantify the CD68 levels in microglia, IBA1 positive cells were selected and CD68 signals within microglia were measured using the region of interest (ROI) tool in ImageJ. To count the Purkinje cell number, lines were drawn along the Purkinje cell layer to measure the distance (mm) using ImageJ, and the number of Purkinje cells along the line was counted by a researcher blinded by the genotypes. The density of the Purkinje cell was calculated as the total cell number/distance. Three brain sections per mouse, separated by 100 μm were used for quantification. The mean from the three sections was used to be representative of each mouse. Data from ≥ 5 brains in each genotype were used for quantification.

For H&E staining, peripheral tissues were collected and perfused with cold PBS. Tissues were post-fixed with 4% PFA, washed with PBS, and stored in 70% ethanol at 4 °C until dehydration for paraffin-embedding. Sectioning and H&E staining were performed on a fee-for-service basis by the Cornell Histology Core Facilities. The white adipocyte size was quantified using the Adiposoft plugins in ImageJ. The percentage of the lipid droplet area in the liver and brown adipose tissue was quantified using ImageJ after thresholding and making binary. Sections from 4 mice in each genotype were quantified.

RNA-seq analysis

Total RNA was extracted from the liver or brain cortex of 10-month-old mice using Trizol (Thermo Scientific). RNA quality was checked using nanodrop, gel electrophoresis, and Agilent Fragment Analyzer. RNAseq libraries were generated by the Cornell TReX Facility using the NEBNext Ultra II Directional RNA Library Prep Kit (New England Biolabs) using 700 ng input total RNA per sample. At least 40 M reads (2 × 150 nt PE) were generated on a NovaSeq (Illumina). Reads were trimmed to remove low-quality and adaptor sequences with TrimGalore (a wrapper for cutadapt and fastQC), requiring a minimum trimmed length of 50 nt. Reads that passed quality control were aligned to reference genome (mouse GRCh38/mm10)¹⁰² using STAR¹⁰³, using ‘--quantMode GeneCounts’ to output counts per gene. SARTools¹⁰⁴ and DESeq2¹⁰⁵ were used to generate normalized counts and perform differential gene expression analysis. Differentially expressed genes (DEGs) were identified by false discovery rates (FDR) or adjusted *p* value ≤ 0.05 using multiple testing with Benjamini-Hochberg correction. All the genes detected in the brain and liver samples were listed in Supplementary Data.1 and 5, respectively.

Heatmap of the DEGs was generated by using Heatmapper¹⁰⁶. Enrichment analysis using the hallmark gene sets or gene ontology biology process (GOBP) was performed using Gene Set Enrichment Analysis (GSEA)¹⁰⁷. The normalized counts of all the expressed genes were uploaded in GSEA and a standard GSEA was run with recommended default settings (1000 gene set permutations). The FDR was estimated to control the false-positive finding of a given normalized enrichment score (NES) by comparing the tails of the observed and null distributions derived from 1000 gene set permutations. The gene sets with absolute normalized enrichment score (NES) > 1.0, nominal *p* value (NOM *p* value) < 0.05, and false discovery rate *q*-value (FDR *q*-value) < 0.1 were considered as significantly enriched. The subset of genes that contributes most to the enrichment result was defined as the core enrichment genes.

Brain lipidomic analysis

To analyze the lipids in the cerebellum, lipids were extracted from 10.0-month-old mouse cerebellum. Total lipids were extracted using a Folch method¹⁰⁸. Briefly, 200 μL of cold solvent mixture (5:2, MeOH:H₂O, v:v) was added to frozen cerebellum tissues and homogenized. Samples were sonicated on ice for 10 min. After sonication, the extra solvent mixture was added based on the tissue weight to make all samples have the same concentration as 0.03 mg/mL. A 150 μL of homogenized sample was transferred

into new tubes and 1000 μL of ice-cold CHCl_3 was added to each sample. The samples were then vortex for 1 h followed by centrifugation at 4 °C with 12,700 rpm for 15 min. The organic solvent layer was transferred into new tubes. Based on the calculated total protein amount, the fraction of organic solvents as much as 200 μg of total protein were dried for lipidomic analysis. EquiSplash® (Avanti Polar Lipids) were used as internal standards (I.S.) and spiked into each tube before drying organic solvents. The I.S. used was listed in Supplementary Table 1. The dried lipids were reconstituted in 150 μL of $\text{MeOH}:\text{CHCl}_3:\text{H}_2\text{O}$ mixture (18:1:1, v/v/v).

Lipidomic analysis was conducted using a Vanquish UHPLC system coupled with a Thermo Scientific Q-Exactive HF-X mass spectrometer. ACQUITY UPLC® BEH Shield RP18 column (1.7 μm , 2.1 \times 150 mm) was used for separation with a 30 min gradient, 0.18 mL/min pump flow rate, and 40 °C column oven temperature. Mobile phase A ($\text{H}_2\text{O}:\text{ACN}$, 9:1, v/v) and mobile phase B ($\text{IPA}:\text{MeOH}:\text{ACN}:\text{H}_2\text{O}$, 7:1.5:1:0.5, v/v/v/v) were used, and 0.5 mM NH_4HCO_2 and 5 mM NH_4OH were used as ionization modifier in both mobile phases. Data-dependent acquisition (DDA) in both positive and negative ion modes was used for lipid identification. Full MS scans with positive and negative ion modes were performed for lipid quantification. The m/z range of MS1 scan was from 380 to 1200 and 380 to 2000 in positive and negative ion modes, respectively. The resolving power was 60 K, automatic gain control (AGC) target was 1E6, normalized collision energy (NCE) was 22.5% (ESI+) or 27.5% (ESI−) with a 10 s and 20 s dynamic exclusion time.

Lipid identification was conducted using Lipidmatch software¹⁰⁹ (v4.0) with 5 ppm mass tolerance for precursor ions and 10 ppm for product ions. All lipid peak areas were normalized using I.S. and total protein amount to calculate their concentration (nmol lipid per mg of total protein). The lipid species identified are listed in Supplementary Data.2. One-way ANOVA with Bonferroni's multiple comparisons was used to determine the significantly changed lipids. Lipids with adjusted p value (FDR) < 0.05 and absolute $\log_2(\text{FC})$ > 0.5 were identified as significantly changed lipids.

Brain proteomic analysis

Mouse cerebellum tissues were first lyophilized briefly to remove the residual buffer, weighted, and homogenized in $\text{MeOH}:\text{H}_2\text{O}$ solvent mixture (5:2, v/v) to precipitate proteins. Proteomics sample preparation was conducted based on our previously described procedures¹¹⁰. Protein pellets were redissolved in lysis buffer (8 M urea, 50 mM ammonium bicarbonate (AmBC), 150 mM NaCl), sonicated on ice for 10 min, and centrifuged (12,700 rpm, 4 °C for 15 min) after drying the protein pellet. Protein concentration was measured using the DC (detergent compatible) protein assay (Bio-Rad) and 40 μg of total proteins was used for the subsequent protein digestion. The Tris(2-carboxyethyl)phosphine (TCEP) (5 mM, for 40 minutes at 37 °C in a Thermomixer (600 rpm)), iodoacetamide (IAA) (15 mM, for 30 min at 37 °C in dark) were used for protein reducing and alkylation, and dithiothreitol (DTT) (5 mM, for 10 min at 37 °C). After dilution of urea concentration below 1 M urea by AmBC (50 mM), trypsin/Lys-C mix (Promega) was used for digestion (1:25, w:w) for 16 h at 37 °C. The trypsin/Lys-C was quenched by trifluoroacetic acid (pH < 2). Peptide samples were washed using a Waters HLB 96-well plate following the manufacturer's protocol. The washed peptide samples were dried, reconstituted in 25 μL 2% acetonitrile with 0.1% formic acid (FA), and clarified by centrifugation. A Dionex Ultimate 3000 RSLCnano system coupled with a Thermo Scientific Q-Exactive HF-X Orbitrap Mass Spectrometer was conducted for proteomics analysis. An Easy-Spray PepMap RSLC C18 column (2 μm , 100 Å, 75 μm \times 50 cm) with 210 min gradient at 55 °C and a flow rate of 0.25 $\mu\text{L}/\text{min}$ was used for peptide separation. The proteomics data analysis was conducted by the Spectronaut software (v19.2, Biognosys) under default settings with DirectDIA mode. The UniProt Mus musculus reviewed database and our custom contaminant protein library¹¹¹ was included for protein identification allowing up to two missed cleavages and three variable modifications. Carbamidomethyl C was used as the fixed modification, and methionine oxidation and protein N-terminal acetylation were used as variable modifications. FDR for precursor peptides and

proteins was set as 0.01 and precursor intensities below 1000 were deleted for better confident identification. All the proteins identified were listed in the Supplementary Data.3. One-way ANOVA with Bonferroni's multiple comparisons was used to determine the significant changed proteins in each comparison. Proteins with FDR < 0.05 and absolute $\log_2(\text{FC})$ > 0.5 were identified as significantly changed proteins.

Liver lipidomic analysis

To analyze the lipids in the liver, lipids were extracted from 20 mg of frozen liver tissues. Total lipids were extracted using a two-step dichloromethane (DCM)/methanol procedure. Briefly, 320 μL cold 50% methanol (v/v) was added to frozen liver tissues and homogenized. Samples were spiked with 30 μL of an internal lipid standard mixture and were sonicated on ice for 10 min. The internal standards used are listed in Supplementary Table 2. Six hundred microliter of DCM was then added to the homogenates and vortexed for 10 s. Three hundred microliter HPLC grade water was then added and vortexed for 10 s, followed by centrifugation at 18,000 rpm for 15 mins at 4 °C. The lower organic layers were collected as lipid extracts. The lipid extracts were evaporated to dryness in a speed vacuum and dissolved in 120 μL acetonitrile (ACN)/isopropanol (IPA)/ H_2O (65:30:5, v/v).

The samples were then analyzed by Vanquish UHPLC coupled with Q-Exactive Hybrid Quadrupole-Orbitrap system (Thermo Fisher Scientific) using a 2.6 μm Accucore C30 column (2.1 mm id \times 150 mm) (Thermo Fisher Scientific) that was held at 55 °C. Solvent flow rate was 260 $\mu\text{L}/\text{min}$ ^{112–114}. The autosampler tray was held at 4 °C and sample injection volume was 2 μL . The following solvents and elution gradients were used. Solvent A: 60% acetonitrile, 40% water, 10 mM ammonium formate with 0.1% formic acid. Solvent B: 90% isopropanol, 10% acetonitrile, 10 mM ammonium formate with 0.1% formic acid. Elution gradient: 0.0–1.5 min (32% B), 1.5–4.0 min (32–45% B), 4.0–5.0 min (45–52% B), 5.0–8.0 min (52–58% B), 8.0–11 min (58–66% B), 11–14 min (66–70% B), 14–18 min (70–75% B), 18–21 min (75–97% B), 21–25 min (97% B), 25–30 min (97–32% B). The QE-HF was operated under data-dependent acquisition with top 15 ions for one survey MS scan for mass range of m/z 250–1200 followed by MS/MS scans on top 15 most intensity peaks. MS survey scans and MS/MS scans were acquired at a resolution of 120,000 and 15,000 (fwhm at m/z 200), respectively. The ESI voltage was 4 kV, the sheath gas flow rate was 50 AU, the auxiliary gas flow rate was 5 AU, and the sweep gas flow rate was 1 AU. The capillary temperature was 320 °C and the auxiliary gas heater temperature was 350 °C. The S-Lens RF level was 60% and all analyses were run in both positive and negative modes.

Data were analyzed using Lipidsearch4.2 software (Thermo Fisher Scientific) to perform normalization, peak alignment and compound identification. Briefly, the data files were searched for product ion MS/MS spectra of lipid precursor ions. MS/MS fragment ions were predicted for all precursor adduct ions measured within ± 5 ppm. The product ions that matched the predicted fragment ions within a ± 5 ppm mass tolerance were used to calculate a match score, and those candidates providing the highest quality match were determined. The search results from the individual positive or negative ion files from each sample group were aligned within a retention time window (± 0.1 min) and the data were merged for each annotated lipid. Finally, the annotated lipids were then filtered to reduce false positives and were normalized using the standards for the different lipid classes. The lipid species identified are listed in Supplementary Data.4. One-way ANOVA with Bonferroni's multiple comparisons was used to determine the significantly changed lipids in each comparison. Lipids with FDR < 0.05 and absolute $\log_2(\text{FC})$ > 0.5 were identified as significantly changed lipids.

Splicing analysis of the TDP-43 targets using RT-qPCR

Total RNAs were extracted from 10-month-old mouse cortex samples using TRIzol (Invitrogen). One microgram of total RNAs was reverse transcribed to cDNA using SuperScript III Reverse Transcriptase (Invitrogen). Quantitative PCR was performed on a LightCycler 480 (Roch Applied Science), and the mRNA levels were measured using efficiency-adjusted $\Delta\Delta\text{-CT}$. The transcripts analyzed were normalized to β -actin. The primers used to detect

the inclusion of *Sort1* exon 17b, *Mapt* exon 2 and 3, and the specific variant of *Sqstm1* identified in TDP-43^{Q331K} mouse brain were from the previous study⁵² and were listed in the Supplementary Table. 3.

Statistics and reproducibility

Statistical analyses were performed using GraphPad Prism 10 except for the omics data. The details about statistics used in different data analyses performed in this study are given in the respective sections of methods and figure legends. Data are presented as mean ± SEM. Statistical significance was assessed by unpaired two-tailed Student's *t*-test (for two-group comparison), one-way ANOVA tests (for multiple comparisons) or two-way ANOVA tests with repeated measures (for the body weight analysis) followed by Bonferroni's multiple comparisons post hoc tests. *P* values less than or equal to 0.05 were considered statistically significant. All lipidomic, RNA-seq, and proteomic analyses were performed by investigators who were blind to the genotypes. The details about the sample sizes and number of replicates in each experiment are given in the respective sections of methods and figure legends.

Reporting summary

Further information on research design is available in the Nature Portfolio Reporting Summary linked to this article.

Data availability

The data supporting the findings of this study are included in the supplemental material. Omics source data are provided in Supplementary Data 1–5. Raw LC-MS/MS data from brain lipidomics and proteomics parts of this manuscript are available through the MassIVE repository (Identifier: MSV000096663). Raw LC-MS/MS data for liver lipidomics are available through the MassIVE repository (Identifier: MSV000096905). Raw RNA-seq data have been deposited at NCBI's Gene Expression Omnibus under the accession number GSE287573. Source data for other graphs are provided in the Supplementary Data 6. Uncropped western blot images are provided in Supplementary Fig. 5. Additional data are available from the corresponding author on request.

Received: 22 April 2024; Accepted: 15 February 2025;

Published online: 26 February 2025

References

- Neumann, M. et al. Ubiquitinated TDP-43 in frontotemporal lobar degeneration and amyotrophic lateral sclerosis. *Science* **314**, 130–133 (2006).
- Wang, I. F., Wu, L. S. & Shen, C. K. TDP-43: an emerging new player in neurodegenerative diseases. *Trends Mol. Med.* **14**, 479–485 (2008).
- Buratti, E. & Baralle, F. E. Multiple roles of TDP-43 in gene expression, splicing regulation, and human disease. *Front. Biosci.* **13**, 867–878 (2008).
- de Boer, E. M. J. et al. TDP-43 proteinopathies: a new wave of neurodegenerative diseases. *J. Neurol. Neurosurg. Psychiatry* **92**, 86–95 (2020).
- Suk, T. R. & Rousseaux, M. W. C. The role of TDP-43 mislocalization in amyotrophic lateral sclerosis. *Mol. Neurodegener.* **15**, 45 (2020).
- Foulds, P. et al. TDP-43 protein in plasma may index TDP-43 brain pathology in Alzheimer's disease and frontotemporal lobar degeneration. *Acta Neuropathol.* **116**, 141–146 (2008).
- Van Deerlin, V. M. et al. Common variants at 7p21 are associated with frontotemporal lobar degeneration with TDP-43 inclusions. *Nat. Genet.* **42**, 234–239 (2010).
- Uryu, K. et al. Concomitant TAR-DNA-binding protein 43 pathology is present in Alzheimer disease and corticobasal degeneration but not in other tauopathies. *J. Neuropathol. Exp. Neurol.* **67**, 555–564 (2008).
- Higashi, S. et al. Concurrence of TDP-43, tau and alpha-synuclein pathology in brains of Alzheimer's disease and dementia with Lewy bodies. *Brain Res.* **1184**, 284–294 (2007).
- Amador-Ortiz, C. et al. TDP-43 immunoreactivity in hippocampal sclerosis and Alzheimer's disease. *Ann. Neurol.* **61**, 435–445 (2007).
- Schwab, C., Arai, T., Hasegawa, M., Yu, S. & McGeer, P. L. Colocalization of transactivation-responsive DNA-binding protein 43 and huntingtin in inclusions of Huntington disease. *J. Neuropathol. Exp. Neurol.* **67**, 1159–1165 (2008).
- Nelson, P. T. et al. Limbic-predominant age-related TDP-43 encephalopathy (LATE): consensus working group report. *Brain* **142**, 1503–1527 (2019).
- Nag, S. & Schneider, J. A. Limbic-predominant age-related TDP43 encephalopathy (LATE) neuropathological change in neurodegenerative diseases. *Nat. Rev. Neurol.* **19**, 525–541 (2023).
- Cruchaga, C. et al. Association of TMEM106B gene polymorphism with age at onset in granulin mutation carriers and plasma granulin protein levels. *Arch. Neurol.* **68**, 581–586 (2011).
- Finch, N. et al. TMEM106B regulates progranulin levels and the penetrance of FTL in GRN mutation carriers. *Neurology* **76**, 467–474 (2011).
- van der Zee, J. et al. TMEM106B is associated with frontotemporal lobar degeneration in a clinically diagnosed patient cohort. *Brain* **134**, 808–815 (2011).
- Deming, Y. & Cruchaga, C. TMEM106B: a strong FTL disease modifier. *Acta Neuropathol.* **127**, 419–422 (2014).
- Gallagher, M. D. et al. TMEM106B is a genetic modifier of frontotemporal lobar degeneration with C9orf72 hexanucleotide repeat expansions. *Acta Neuropathol.* **127**, 407–418 (2014).
- Lattante, S. et al. Defining the association of TMEM106B variants among frontotemporal lobar degeneration patients with GRN mutations and C9orf72 repeat expansions. *Neurobiol. Aging* **35**, 2658 e2651–2658 e2655 (2014).
- van Blitterswijk, M. et al. TMEM106B protects C9ORF72 expansion carriers against frontotemporal dementia. *Acta Neuropathol.* **127**, 397–406 (2014).
- Cherry, J. D. et al. Variation in TMEM106B in chronic traumatic encephalopathy. *Acta Neuropathol. Commun.* **6**, 115 (2018).
- Bieniek, K. F. et al. Chronic traumatic encephalopathy pathology in a neurodegenerative disorders brain bank. *Acta Neuropathol.* **130**, 877–889 (2015).
- Nelson, P. T. et al. Reassessment of risk genotypes (GRN, TMEM106B, and ABCC9 variants) associated with hippocampal sclerosis of aging pathology. *J. Neuropathol. Exp. Neurol.* **74**, 75–84 (2015).
- Yu, L. et al. The TMEM106B locus and TDP-43 pathology in older persons without FTL. *Neurology* **84**, 927–934 (2015).
- Rhinn, H. & Abeliovich, A. Differential aging analysis in human cerebral cortex identifies variants in TMEM106B and GRN that regulate aging phenotypes. *Cell Syst.* **4**, 404–415 e405 (2017).
- Simons, C. et al. A recurrent de novo mutation in TMEM106B causes hypomyelinating leukodystrophy. *Brain* **140**, 3105–3111 (2017).
- Yan, H. et al. The recurrent mutation in TMEM106B also causes hypomyelinating leukodystrophy in China and is a CpG hot spot. *Brain* **141**, e36 (2018).
- Perneel, J. et al. Accumulation of TMEM106B C-terminal fragments in neurodegenerative disease and aging. *Acta Neuropathol.* **145**, 285–302 (2023).
- Schweighauser, M. et al. Age-dependent formation of TMEM106B amyloid filaments in human brains. *Nature* **605**, 310–314 (2022).
- Perneel, J. & Rademakers, R. Identification of TMEM106B amyloid fibrils provides an updated view of TMEM106B biology in health and disease. *Acta Neuropathol.* **144**, 807–819 (2022).
- Jiang, Y. X. et al. Amyloid fibrils in FTL-TDP are composed of TMEM106B and not TDP-43. *Nature* **605**, 304–309 (2022).

32. Fan, Y. et al. Generic amyloid fibrillation of TMEM106B in patients with Parkinson's disease dementia and normal elders. *Cell Res.* **32**, 585–588 (2022).
33. Copley, K. E. & Shorter, J. Flying under the radar: TMEM106B(120–254) fibrils break out in diverse neurodegenerative disorders. *Cell* **185**, 1290–1292 (2022).
34. Chang, A. et al. Homotypic fibrillization of TMEM106B across diverse neurodegenerative diseases. *Cell* **185**, 1346–1355 e1315 (2022).
35. Stagi, M., Klein, Z. A., Gould, T. J., Bewersdorf, J. & Strittmatter, S. M. Lysosome size, motility and stress response regulated by frontotemporal dementia modifier TMEM106B. *Mol. Cell Neurosci.* **61**, 226–240 (2014).
36. Brady, O. A., Zheng, Y., Murphy, K., Huang, M. & Hu, F. The frontotemporal lobar degeneration risk factor, TMEM106B, regulates lysosomal morphology and function. *Hum. Mol. Genet.* **22**, 685–695 (2013).
37. Lang, C. M. et al. Membrane orientation and subcellular localization of transmembrane protein 106B (TMEM106B), a major risk factor for frontotemporal lobar degeneration. *J. Biol. Chem.* **287**, 19355–19365 (2012).
38. Chen-Plotkin, A. S. et al. TMEM106B, the risk gene for frontotemporal dementia, is regulated by the microRNA-132/212 cluster and affects progranulin pathways. *J. Neurosci.* **32**, 11213–11227 (2012).
39. Klein, Z. A. et al. Loss of TMEM106B ameliorates lysosomal and frontotemporal dementia-related phenotypes in progranulin-deficient mice. *Neuron* **95**, 281–296 e286 (2017).
40. Kundu, S. T. et al. TMEM106B drives lung cancer metastasis by inducing TFEB-dependent lysosome synthesis and secretion of cathepsins. *Nat. Commun.* **9**, 2731 (2018).
41. Luningschror, P. et al. The FTL risk factor TMEM106B regulates the transport of lysosomes at the axon initial segment of motoneurons. *Cell Rep.* **30**, 3506–3519 e3506 (2020).
42. Feng, T. et al. A role of the frontotemporal lobar degeneration risk factor TMEM106B in myelination. *Brain* **143**, 2255–2271 (2020).
43. Schwenk, B. M. et al. The FTL risk factor TMEM106B and MAP6 control dendritic trafficking of lysosomes. *EMBO J.* **33**, 450–467 (2014).
44. Feng, T. et al. TMEM106B deficiency impairs cerebellar myelination and synaptic integrity with Purkinje cell loss. *Acta Neuropathol. Commun.* **10**, 33 (2022).
45. Feng, T. et al. Loss of TMEM106B and PGRN leads to severe lysosomal abnormalities and neurodegeneration in mice. *EMBO Rep.* **21**, e50219 (2020).
46. Levine, T. P. TMEM106B in humans and Vac7 and Tag1 in yeast are predicted to be lipid transfer proteins. *Proteins* **90**, 164–175 (2022).
47. Marks, J. D. et al. TMEM106B core deposition associates with TDP-43 pathology and is increased in risk SNP carriers for frontotemporal dementia. *Sci. Transl. Med.* **16**, eadf9735 (2024).
48. Mao, F. et al. TMEM106B modifies TDP-43 pathology in human ALS brain and cell-based models of TDP-43 proteinopathy. *Acta Neuropathol.* **142**, 629–642 (2021).
49. Sreedharan, J. et al. TDP-43 mutations in familial and sporadic amyotrophic lateral sclerosis. *Science* **319**, 1668–1672 (2008).
50. Rutherford, N. J. et al. Novel mutations in TARDBP (TDP-43) in patients with familial amyotrophic lateral sclerosis. *PLoS Genet.* **4**, e1000193 (2008).
51. Buratti, E. Functional significance of TDP-43 mutations in disease. *Adv. Genet.* **91**, 1–53 (2015).
52. White, M. A. et al. TDP-43 gains function due to perturbed autoregulation in a Tardbp knock-in mouse model of ALS-FTD. *Nat. Neurosci.* **21**, 552–563 (2018).
53. Scotter, E. L., Chen, H. J. & Shaw, C. E. TDP-43 proteinopathy and ALS: insights into disease mechanisms and therapeutic targets. *Neurotherapeutics* **12**, 352–363 (2015).
54. Zhou, X. et al. Loss of TMEM106B leads to myelination deficits: implications for frontotemporal dementia treatment strategies. *Brain* **143**, 1905–1919 (2020).
55. Zhao, J., Zhang, H., Fan, X., Yu, X. & Huai, J. Lipid Dyshomeostasis and Inherited Cerebellar Ataxia. *Mol. Neurobiol.* **59**, 3800–3828 (2022).
56. Zhou, Y. et al. Altered lipid homeostasis is associated with cerebellar neurodegeneration in SNX14 deficiency. *JCI Insight* **9** <https://doi.org/10.1172/jci.insight.168594> (2024).
57. Takahashi, H. et al. Lysosomal TMEM106B interacts with galactosylceramidase to regulate myelin lipid metabolism. *Commun. Biol.* **7**, 1088 (2024).
58. Lee, J. Y. et al. The major TMEM106B dementia risk allele affects TMEM106B protein levels, fibril formation, and myelin lipid homeostasis in the ageing human hippocampus. *Mol. Neurodegener.* **18**, 63 (2023).
59. Tucic, M., Stamenkovic, V. & Andjus, P. The extracellular matrix glycoprotein tenascin C and adult neurogenesis. *Front Cell Dev. Biol.* **9**, 674199 (2021).
60. Sekeljic, V. & Andjus, P. R. Tenascin-C and its functions in neuronal plasticity. *Int J. Biochem Cell Biol.* **44**, 825–829 (2012).
61. Barski, J. J. et al. Calbindin in cerebellar Purkinje cells is a critical determinant of the precision of motor coordination. *J. Neurosci.* **23**, 3469–3477 (2003).
62. Ishikawa, K. et al. Calbindin-D 28k immunoreactivity in the cerebellum of spinocerebellar degeneration. *J. Neurol. Sci.* **129**, 179–185 (1995).
63. Alonso, I. et al. A novel H101Q mutation causes PKCgamma loss in spinocerebellar ataxia type 14. *J. Hum. Genet.* **50**, 523–529 (2005).
64. Chopra, R., Wasserman, A. H., Pulst, S. M., De Zeeuw, C. I. & Shakkottai, V. G. Protein kinase C activity is a protective modifier of Purkinje neuron degeneration in cerebellar ataxia. *Hum. Mol. Genet.* **27**, 1396–1410 (2018).
65. Turkmen, S. et al. CA8 mutations cause a novel syndrome characterized by ataxia and mild mental retardation with predisposition to quadrupedal gait. *PLoS Genet.* **5**, e1000487 (2009).
66. Kaiyrzhanov, R. et al. Clinical and molecular spectrum of autosomal recessive CA8-related cerebellar ataxia. *Move. Disord.* **39**, 983–995 (2024).
67. Jiang, L. & Ngo, S. T. Altered TDP-43 Structure and function: key insights into aberrant RNA, mitochondrial, and cellular and systemic metabolism in amyotrophic lateral sclerosis. *Metabolites* **12** <https://doi.org/10.3390/metabo12080709> (2022).
68. Anwar, S. D., Foster, C. & Ashraf, A. Lipid disorders and metabolic-associated fatty liver disease. *Endocrinol. Metab. Clin. North Am.* **52**, 445–457 (2023).
69. Feng, T., Lacrampe, A. & Hu, F. Physiological and pathological functions of TMEM106B: a gene associated with brain aging and multiple brain disorders. *Acta Neuropathol.* **141**, 327–339 (2021).
70. Root, J., Merino, P., Nuckols, A., Johnson, M. & Kukar, T. Lysosome dysfunction as a cause of neurodegenerative diseases: lessons from frontotemporal dementia and amyotrophic lateral sclerosis. *Neurobiol. Dis.* **154**, 105360 (2021).
71. Tan, R. H. et al. Cerebellar neuronal loss in amyotrophic lateral sclerosis cases with ATXN2 intermediate repeat expansions. *Ann. Neurol.* **79**, 295–305 (2016).
72. Liu, Y. et al. Hyperactivity of Purkinje cell and motor deficits in C9orf72 knockout mice. *Mol. Cell Neurosci.* **121**, 103756 (2022).
73. Chew, J. et al. Neurodegeneration. C9ORF72 repeat expansions in mice cause TDP-43 pathology, neuronal loss, and behavioral deficits. *Science* **348**, 1151–1154 (2015).
74. Todd, T. W. et al. Hexanucleotide repeat expansions in c9FTD/ALS and SCA36 confer selective patterns of neurodegeneration in vivo. *Cell Rep.* **31**, 107616 (2020).

75. Popa, L. S., Streng, M. L. & Ebner, T. J. Purkinje cell representations of behavior: diary of a busy neuron. *Neuroscientist* **25**, 241–257 (2019).
76. Rademakers, R. et al. Loss of Tmem106b leads to cerebellum Purkinje cell death and motor deficits. *Brain Pathol.* **31**, e12945 (2021).
77. Stroobants, S., D’Hooge, R. & Damme, M. Aged Tmem106b knockout mice display gait deficits in coincidence with Purkinje cell loss and only limited signs of non-motor dysfunction. *Brain Pathol.* **31**, 223–238 (2021).
78. Faissner, A., Roll, L. & Theodoridis, U. Tenascin-C in the matrisome of neural stem and progenitor cells. *Mol. Cell Neurosci.* **81**, 22–31 (2017).
79. Jakovljevic, A. et al. The role of tenascin-c on the structural plasticity of perineuronal nets and synaptic expression in the hippocampus of male mice. *Biomolecules* **14** <https://doi.org/10.3390/biom14040508> (2024).
80. Chiang, P. M. et al. Deletion of TDP-43 down-regulates Tbc1d1, a gene linked to obesity, and alters body fat metabolism. *Proc. Natl. Acad. Sci. USA* **107**, 16320–16324 (2010).
81. Stallings, N. R. et al. TDP-43, an ALS linked protein, regulates fat deposition and glucose homeostasis. *PLoS ONE* **8**, e71793 (2013).
82. Arnold, E. S. et al. ALS-linked TDP-43 mutations produce aberrant RNA splicing and adult-onset motor neuron disease without aggregation or loss of nuclear TDP-43. *Proc. Natl. Acad. Sci. USA* **110**, E736–E745 (2013).
83. Chew, H., Solomon, V. A. & Fonteh, A. N. Involvement of lipids in Alzheimer’s disease pathology and potential therapies. *Front Physiol.* **11**, 598 (2020).
84. Yin, F. Lipid metabolism and Alzheimer’s disease: clinical evidence, mechanistic link and therapeutic promise. *FEBS J.* **290**, 1420–1453 (2023).
85. Godoy-Corchuelo, J. M. et al. Lipid Metabolic alterations in the ALS-FTD spectrum of disorders. *Biomedicine* **10** <https://doi.org/10.3390/biomedicine10051105> (2022).
86. Marian, O. C. et al. Disrupted myelin lipid metabolism differentiates frontotemporal dementia caused by GRN and C9orf72 gene mutations. *Acta Neuropathol. Commun.* **11**, 52 (2023).
87. Maksimovic, K., Youssef, M., You, J., Sung, H. K. & Park, J. Evidence of metabolic dysfunction in amyotrophic lateral sclerosis (ALS) patients and animal models. *Biomolecules* **13** <https://doi.org/10.3390/biom13050863> (2023).
88. Agrawal, I., Lim, Y. S., Ng, S. Y. & Ling, S. C. Deciphering lipid dysregulation in ALS: from mechanisms to translational medicine. *Transl. Neurodegener.* **11**, 48 (2022).
89. Mahuran, D. J. Biochemical consequences of mutations causing the GM2 gangliosidosis. *Biochim. Biophys. Acta* **1455**, 105–138 (1999).
90. Kowalewski, B. et al. Molecular characterization of arylsulfatase G: expression, processing, glycosylation, transport, and activity. *J. Biol. Chem.* **289**, 27992–28005 (2014).
91. Huang, Y. & Mahley, R. W. Apolipoprotein E: structure and function in lipid metabolism, neurobiology, and Alzheimer’s diseases. *Neurobiol. Dis.* **72**, 3–12 (2014).
92. Rodriguez-Agudo, D. et al. StarD5: an ER stress protein regulates plasma membrane and intracellular cholesterol homeostasis. *J. Lipid Res.* **60**, 1087–1098 (2019).
93. Shirane, M. Pathogenic contribution of cholesteryl ester accumulation in the brain to neurodegenerative disorders. *Neural Regen. Res.* **19**, 2099–2100 (2024).
94. Singh, S. et al. PLD3 and PLD4 synthesize SS-BMP a key phospholipid enabling lipid degradation in lysosomes. *Cell* **187**, 6820–6834.e24 (2024).
95. Fernandez-Eulate, G. et al. A comprehensive serum lipidome profiling of amyotrophic lateral sclerosis. *Amyotroph. Lateral Scler. Frontotemporal Degener.* **21**, 252–262 (2020).
96. Sol, J. et al. Lipidomic traits of plasma and cerebrospinal fluid in amyotrophic lateral sclerosis correlate with disease progression. *Brain Commun.* **3**, fcab143 (2021).
97. Area-Gomez, E. et al. Lipidomics study of plasma from patients suggest that ALS and PLS are part of a continuum of motor neuron disorders. *Sci. Rep.* **11**, 13562 (2021).
98. Andres-Benito, P. et al. Lipid alterations in human frontal cortex in ALS-FTLD-TDP43 proteinopathy spectrum are partly related to peroxisome impairment. *Neuropathol. Appl. Neurobiol.* **47**, 544–563 (2021).
99. Stribl, C. et al. Mitochondrial dysfunction and decrease in body weight of a transgenic knock-in mouse model for TDP-43. *J. Biol. Chem.* **289**, 10769–10784 (2014).
100. Luikinga, S. et al. Profound lipid dysregulation in mutant TDP-43 mice is ameliorated by the glucocerebrosidase 2 inhibitor ambroxol. *bioRxiv*, 2022.2008.2030.505901. <https://doi.org/10.1101/2022.08.30.505901> (2022).
101. Miedel, C. J., Patton, J. M., Miedel, A. N., Miedel, E. S. & Levenson, J. M. Assessment of spontaneous alternation, novel object recognition and limb clasping in transgenic mouse models of amyloid-beta and tau neuropathology. *J. Vis. Exp.* <https://doi.org/10.3791/55523> (2017).
102. Zerbino, D. R. et al. Ensembl 2018. *Nucleic Acids Res.* **46**, D754–D761 (2018).
103. Dobin, A. et al. STAR: ultrafast universal RNA-seq aligner. *Bioinformatics* **29**, 15–21 (2013).
104. Varet, H., Brillet-Gueguen, L., Coppee, J. Y. & Dillies, M. A. SARTools: a DESeq2- and EdgeR-based R pipeline for comprehensive differential analysis of RNA-Seq data. *PLoS ONE* **11**, e0157022 (2016).
105. Love, M. I., Huber, W. & Anders, S. Moderated estimation of fold change and dispersion for RNA-seq data with DESeq2. *Genome Biol.* **15**, 550 (2014).
106. Babicki, S. et al. Heatmapper: web-enabled heat mapping for all. *Nucleic Acids Res.* **44**, W147–W153 (2016).
107. Subramanian, A. et al. Gene set enrichment analysis: a knowledge-based approach for interpreting genome-wide expression profiles. *Proc. Natl. Acad. Sci. USA* **102**, 15545–15550 (2005).
108. Folch, J., Lees, M. & Sloane Stanley, G. H. A simple method for the isolation and purification of total lipides from animal tissues. *J. Biol. Chem.* **226**, 497–509 (1957).
109. Koelmel, J. P. et al. LipidMatch: an automated workflow for rule-based lipid identification using untargeted high-resolution tandem mass spectrometry data. *BMC Bioinform.* **18**, 331 (2017).
110. Lee, G. B., Mazli, W. & Hao, L. Multiomics evaluation of human iPSCs and iPSC-derived neurons. *J. Proteome Res.* **23**, 3149–3160 (2024).
111. Frankenfield, A. M., Ni, J., Ahmed, M. & Hao, L. Protein contaminants matter: building universal protein contaminant libraries for DDA and DIA proteomics. *J. Proteome Res.* **21**, 2104–2113 (2022).
112. Bhawal, R., Fu, Q., Anderson, E. T., Gibson, G. E. & Zhang, S. Serum metabolomic and lipidomic profiling reveals novel biomarkers of efficacy for benfotiamine in Alzheimer’s disease. *Int. J. Mol. Sci.* **22** <https://doi.org/10.3390/ijms222413188> (2021).
113. Vidavsky, N. et al. Mapping and profiling lipid distribution in a 3D model of breast cancer progression. *ACS Cent. Sci.* **5**, 768–780 (2019).
114. Montague, B. et al. Identifying potential biomarkers and therapeutic targets for dogs with sepsis using metabolomics and lipidomics analyses. *PLoS ONE* **17**, e0271137 (2022).

Acknowledgements

We thank Sara Down and Dr. Jeff Pleiss for their help with RNA splicing analysis. We thank Ms. Xiaochun Wu for her technical assistance and Dr. Chris Schaffer, Dr. Nozomi Nishimura, and Dr. Matthew David Isaacson for their assistance with behavioral tests. This work is supported by NINDS/NIA (R01NS088448 & R21AG078741) to F.H., R01NS121608 to L.H., and the Weill Institute Fleming Postdoctoral Fellowship to C.Y.

Author contributions

C.Y. performed the experiments, analyzed the data, and drafted the manuscript. G.L. performed lipidomic and proteomic analysis of cerebellum samples and helped with omic statistical analysis under the supervision of L.H. and F.H. supervised the project and edited the manuscript. All authors read and approved the final manuscript.

Competing interests

The authors declare no competing interests.

Ethical approval

All applicable international, national, and/or institutional guidelines for the care and use of animals were followed. The work under animal protocol 2017-0056 is approved by the Institutional Animal Care and Use Committee at Cornell University.

Additional information

Supplementary information The online version contains supplementary material available at <https://doi.org/10.1038/s42003-025-07752-2>.

Correspondence and requests for materials should be addressed to Fenghua Hu.

Peer review information *Communications Biology* thanks the anonymous reviewers for their contribution to the peer review of this work. Primary Handling Editors: Christopher Hine and Dario Ummarino. A peer review file is available.

Reprints and permissions information is available at <http://www.nature.com/reprints>

Publisher's note Springer Nature remains neutral with regard to jurisdictional claims in published maps and institutional affiliations.

Open Access This article is licensed under a Creative Commons Attribution-NonCommercial-NoDerivatives 4.0 International License, which permits any non-commercial use, sharing, distribution and reproduction in any medium or format, as long as you give appropriate credit to the original author(s) and the source, provide a link to the Creative Commons licence, and indicate if you modified the licensed material. You do not have permission under this licence to share adapted material derived from this article or parts of it. The images or other third party material in this article are included in the article's Creative Commons licence, unless indicated otherwise in a credit line to the material. If material is not included in the article's Creative Commons licence and your intended use is not permitted by statutory regulation or exceeds the permitted use, you will need to obtain permission directly from the copyright holder. To view a copy of this licence, visit <http://creativecommons.org/licenses/by-nc-nd/4.0/>.

© The Author(s) 2025